Title:

A long duration of the ^{16}O-rich reservoir in the solar nebula, as recorded in fine-grained refractory inclusions from the least metamorphosed carbonaceous chondrites.

Authors:

Takayuki Ushikubo [1,2*], Travis J. Tenner [1,3], Hajime Hiyagon [4], and Noriko T. Kita [1]

Affiliations:
1: WiscSIMS, Department of Geoscience, University of Wisconsin-Madison, 1215 W. Dayton St., Madison, WI 53706 USA
2: Kochi Institute for Core Sample Research, Japan Agency for Marine-Earth Science and Technology (JAMSTEC), 200 Monobe-otsu, Nankoku, Kochi 783-8502 Japan
3: Chemistry Division, Nuclear and Radiochemistry, Los Alamos National Laboratory, MS J514, Los Alamos, NM 87545 USA
4: Department of Earth and Planetary Science, Graduate school of Science, University of Tokyo, 7-3-1 Hongo, Bunkyo, Tokyo 113-0033 Japan

*: Corresponding author:
Takayuki Ushikubo (ushikubot@jamstec.go.jp)
Kochi Institute for Core Sample Research, Japan Agency for Marine-Earth Science and Technology (JAMSTEC), 200 Monobe-otsu, Nankoku, Kochi 783-8502 Japan
Phone: +81-088-878-2187

Submitted to GCA, revised manuscript

Abstract

Oxygen isotope ratios and corresponding ^{26}Al-^{26}Mg isotope systematics of refractory inclusions from the least metamorphosed carbonaceous chondrites, Acfer 094 (C-ungrouped 3.00) and Yamato 81020 (CO3.05), were measured with an ion microprobe. Most of the samples are fine-grained refractory inclusions which are considered as condensates from high temperature Solar Nebular gas. The refractory inclusions consistently exhibit ^{16}O-enriched signatures among their interior phases (spinel, melilite, and high-Ca pyroxene), as well as phases within their rim structures (spinel, high-Ca pyroxene, and adjacent anorthite). This observation indicates that aggregated refractory condensates and the formation of rim structures occurred in the same ^{16}O-rich environment. Evidence for mass-dependent isotopic fractionation in oxygen and magnesium, which would indicate a later flash heating process, was not observed in rims. All oxygen isotope data from fine-grained CAIs are distributed between the Carbonaceous Chondrite Anhydrous Mineral (CCAM) line and the Primitive Chondrule Mineral (PCM) regression line based on oxygen isotope data from Acfer 094 chondrules. The inferred initial ^{26}Al/^{27}Al ratios, (^{26}Al/^{27}Al)$_0$, of spinel-melilite-rich CAIs are $(4.08\pm0.75)\times10^{-5}$ to $(5.05\pm0.18)\times10^{-5}$ (errors are 2σ), which are slightly lower than the canonical value of 5.25×10^{-5}. As there is no petrologic evidence for re-melting after condensation, the lower (^{26}Al/^{27}Al)$_0$ values of these CAIs indicate either they formed up to ~0.3 Ma after canonical CAIs or they formed before ^{26}Al was homogeneously distributed in the Solar nebula. A pyroxene-anorthite-rich CAI, G92, has an ^{16}O-rich signature like other CAIs but also has an order-of-magnitude less ^{26}Mg-excess in anorthite, corresponding to a (^{26}Al/^{27}Al)$_0$ of $(5.21\pm0.54)\times10^{-6}$. As there is no evidence for a later Mg isotopic disturbance, G92 anorthite is interpreted to have formed by interaction with ^{16}O-rich nebular gas at 2 to 3 Ma after CAI formation. With the observation that ^{16}O-rich refractory inclusions, relatively ^{16}O-poor chondrules, and extremely ^{16}O-poor cosmic symplectites within Acfer 094 all plot on the PCM line, it suggests that ^{16}O-rich nebular gas and extremely ^{16}O-poor primordial volatiles represent mass-independent fractionated endmembers in the early Solar system and that the PCM line represents a mixing line of these two endmembers.

1. Introduction

In the early Solar System, evidence for an ^{16}O-rich isotopic signature that fractionated independent of mass ($\Delta^{17}\mathrm{O} \equiv \delta^{17}\mathrm{O} - 0.52 \times \delta^{18}\mathrm{O} \sim -24‰$) has been found in Ca-, Al-rich inclusions (CAIs) and amoeboid olivine aggregates (AOAs) (Clayton et al., 1977; Hiyagon and Hashimoto, 1999; Krot et al., 2002; 2010a). As refractory inclusions (CAIs and AOAs) are commonly interpreted to be the first solar system condensates (Grossman, 1972; Grossman et al., 2008), their oxygen isotope ratios are inferred to reflect the primordial characteristics of the earliest refractory dust forming environment in the solar nebula. In contrast, oxygen isotope ratios of chondrules that formed ~2 million years (Ma) after CAIs (Kita and Ushikubo, 2012; Kita et al., 2013; Ushikubo et al., 2013) have a smaller mass-independent oxygen isotopic anomaly relative to CAIs, indicating a later oxygen isotope environment that was relatively ^{16}O-poor (e.g., Clayton et al., 1983; Clayton 2003; Connolly and Huss, 2010; Kita et al., 2010; Krot et al., 2010b; Rudraswami et al., 2011; Weisberg et al., 2011; Nakashima et al., 2012; Ushikubo et al., 2012; Schrader et al., 2013, 2014; Tenner et al., 2013, 2015).

Since some CAIs exhibit evidence for later re-heating processes after their initial formation, including significant differences in Δ^{17}O values between primary phases and secondary phases (Yurimoto et al., 1998; Hsu et al., 2000; Fagan et al., 2007; Ushikubo et al., 2007; Krot et al., 2008; MacPherson et al., 2012; Kawasaki et al., 2015), they are expected to record temporal changes of oxygen isotope environments within the solar nebula. In addition, detailed petrologic and isotopic studies of fine-textured Wark-Lovering rims surrounding coarse-grained CAIs, which consists of (1) a spinel layer with minor perovskite and hibonite (inner part); (2) a melilite/anorthite/secondary altered phase layer (middle part); and (3) a Ti-Al-bearing diopside layer (outer part) (Wark and Lovering, 1977), suggest that variability in oxygen isotope ratios existed when the Wark and Lovering rims formed (e.g., Yoshitake et al., 2005; Simon et al., 2011, 2016). Impartantly, however, Bodénan et al. (2014) observed that such an oxygen isotopic variability is not recognized among Wark-Lovering rims from pristine carbonaceous chondrite CAIs. This suggests that the oxygen isotopic variability found in the aforementioned studies, from which refractory inclusions from higher petrologic type chondrites were investigated, could be due to later isotopic disturbances in chondritic parent bodies. If oxygen isotopic variability (^{16}O-rich and ^{16}O-poor environments) existed in the early solar system when coarse-grained CAIs and Wark-Lovering rim formed, it is expected that evidence for oxygen isotopic variability would also be recorded within fine-grained CAIs and AOAs (Grossman and Ganapathy, 1976; Grossman and Steele, 1976).

Although coarse-grained CAIs are advantageous for in-situ high-precision isotope analyses, they experienced re-melting after aggregation of precursor dust condensates and they commonly have positively fractionated Mg and Si isotope ratios. As positive isotopic fractionation in Mg and Si provides evidence for significant evaporative loss by re-melting, primary oxygen isotope ratios of such coarse-grained CAIs are probably modified (e.g., Wang et al., 2001; Alexander, 2004). In contrast, the texture of fine-grained CAIs and AOAs (e.g., small grain sizes of major phases and complex nodules) indicates that they formed by aggregation of primary condensates from early solar nebular gas. As such, fine-grained CAIs and AOAs are perhaps the best candidates for recording pristine oxygen isotope ratios of early solar system condensates. However, the petrology and isotopic compositions of such fine-scale materials are particularly susceptible to metamorphism while on chondritic parent bodies. Thus, in order to establish that isotope signatures of fine-grained refractory inclusions are indeed primordial nebular signatures, selection of pristine CAIs and AOAs that properly rule out evidence for parent body metamorphism is critically important.

In this study, we measured oxygen isotope ratios and ^{26}Al-^{26}Mg systematics of fine-grained CAIs and AOAs from Acfer 094 (C-ungrouped 3.00) and Yamato-81020 (Y-81020, CO3.05). These refractory inclusions should record pristine isotope characteristics because Acfer 094 and Y-81020 are two of the least metamorphosed carbonaceous chondrites (Grossman and Brearley, 2005; Kimura et al., 2008). For example, Acfer 094 chondrules preserve intrinsic oxygen isotope ratios without any indication of a later oxygen isotopic disturbance, even in mesostasis glass that is highly sensitive to fluid assisted parent body metamorphism (Ushikubo et al., 2012). In addition, chondrules from both Acfer 094 and Y-81020 have ^{26}Al-^{26}Mg isotope systematics that are primary, with no sign of a later disturbance (Kunihiro et al., 2004; Kurahashi et al., 2008; Hutcheon et al., 2009; Ushikubo et al., 2013). Thus, oxygen isotope ratios and ^{26}Al-^{26}Mg isotope systematics of fine-grained refractory inclusions from the same meteorites should dependably elucidate the evolution of oxygen isotope ratios in the solar nebula, recording their formation and interaction with ambient gas before accreting to the chondritic parent body.

2. Samples

Ten refractory inclusions, including five spinel-melilite-rich CAIs (G5, G16, G49, G104, and Y81020-E-8), one pyroxene-anorthite-rich CAI (G92), and four AOAs (G17, G28, G44, and G58) were selected for investigation by secondary ion mass spectrometry (SIMS) (Figs. 1-3). Y81020-E-8 is from Y-81020 (CO3.05) and the others are from Acfer 094 (C-ungrouped 3.00). The classification of Acfer 094 refractory inclusions by Krot et al. (2004a) is applied in this study.

Three of the five spinel-melilite-rich CAIs (G5, G16, and G49) have a fine-grained, complex nodular texture. CAI G5 is an irregular-shaped aggregate of multiple nodules (Fig. 1a). It consists of gehlenitic melilite (Åk$_{6}$) and spinel, along with anorthite and diopside rims. Some nodules do not contain melilite. CAI G16 is a large CAI (ca. 300 μm × 500 μm in size, Fig. 1b) consisting of multiple nodules. The larger nodules consist of melilite (Åk$_{8-10}$) and sub-micron spinel grains surrounded by a diopside rim (Fig. 1f). Regarding the smaller nodules, spinel is rare, a thin anorthite layer commonly occurs between the interior melilite and the diopside rim, and olivine grains are found in the accretionary rim (Fig. 1g). CAI G49 is an irregular-shaped aggregate of small nodules, consisting of melilite (Åk$_{20}$), tiny spinel and Al-Ti-rich diopside grains, and a diopside rim (Fig. 1c). A thin anorthite layer between the interior melilite and the diopside rim is also present in nodules near the edge of this CAI.

The remaining two spinel-melilite-rich CAIs have relatively simple textures and larger grain sizes. CAI G104 is a fragment of an irregular-shaped spinel-melilite-rich CAI (Fig. 1d). It consists of melilite (Åk$_{8}$), spinel, Al-Ti-rich diopside, and perovskite. Thin spinel (discontinuous and <2 μm) and diopside (<5 μm) layers are observed along the rim. There are several voids in melilite and interstitial space of spinel grains. Al-Ti-rich diopside and perovskite commonly occur around these voids (Fig. 1h).

CAI Y81020-E-8 is round and ~500 μm in diameter (Fig. 1e). It consists mostly of melilite (Åk$_{14-21}$), spinel, and perovskite. The central portion of this CAI has likely been lost during sample preparation. Y81020-E-8 is surrounded a double-layered rim of spinel (10 to 30 μm in width) and melilite (~5 μm in width); a diopside rim appears to be absent (Fig. 1i).

CAI G92 is an irregular-shaped pyroxene-anorthite-rich CAI that is 300 μm × 150 μm in size. It consists of anorthite and Al-Ti-rich diopside, with small amounts of melilite (Åk$_{19-25}$) and spinel (Fig. 2a). Al-Ti-rich diopside is often associated with voids (Fig. 2b). A thin diopside rim (~3 μm) is also observed. Anhedral melilite and Al-Ti-rich diopside (typically <10 μm in size) are enclosed by anorthite. Spinel (typically <3 μm in size) occurs either in melilite or near the diopside rim. No ferromagnesian phases, such as olivine or low-Ca pyroxene, are observed outside of the diopside rim.

All AOAs studied consist of multiple Ca-, Al-rich domains enclosed by olivine. Among them, Ca-, Al-rich domains of G17 (~200 μm × 100 μm in size, Fig. 3a) and G28 (~400 μm × 300 μm in size, Fig. 3b) consist of spinel and Al-Ti-rich diopside but almost no anorthite (Fig. 3e). In contrast, Ca-, Al-rich domains of fragment G44 (~200 μm × 150 μm in size, Fig. 3c) and G58 (~400 μm × 300 μm in size, Fig. 3d) consist of spinel, anorthite, and Al-Ti-rich diopside (Fig.3f).

3. Analytical procedures

3.1. SEM observation and major element analysis by EPMA

Backscattered electron (BSE) and secondary electron images were obtained by the Hitachi S-3400 scanning electron microscope (SEM) at University of Wisconsin-Madison (UW-Madison). Major element oxide (SiO_2, TiO_2, Al_2O_3, Cr_2O_3, FeO, MnO, MgO, CaO, Na_2O, and V_2O_5) concentrations of minerals were obtained with the CAMECA SX51 electron-probe microanalyzer (EPMA) at UW-Madison using a 15 kV accelerating voltage, a 10 nA beam current, a fully focused beam, and respective peak and background counting times of 10 and 5 s. Standards consisted of olivine ($Fo_{0,\ 83,\ 89,\ 100}$), pyroxene (enstatite, wollastonite, augite, jadeite), plagioclase ($An_{0,\ 18,\ 78,\ 95}$), gehlenite, åkermanite, spinel (Mg-endmember, intermediate Mg-Fe endmember, and chromium-spinel), rutile, hornblende, chromite, hematite, magnetite, tephroite, and V-metal. Calculated detection limits (at 99% confidence) were 0.02, 0.03, 0.02, 0.07, 0.05, 0.05, 0.03, 0.03, 0.04, and 0.07 wt%, respectively for the oxides listed above.

3.2 Isotope analysis by SIMS

Oxygen three-isotopes and ^{26}Al-^{26}Mg isotope systematics were measured using the WiscSIMS CAMECA IMS-1280 Secondary Ion Mass Spectrometer (SIMS) at the University of Wisconsin-Madison. Four separate sessions (i.e., O and Mg isotope analyses with different beam diameters) were conducted, in order to obtain isotopic signatures of multiple phases that have a range of grain sizes among individual refractory inclusions.

After each analytical session, SIMS pits were assessed by SEM and data from pits with irregularities (e.g., overlapping multiple phases, cracks, or inclusions) were rejected.

3.2.1 Oxygen three-isotope analysis

For oxygen three-isotope analysis, a $^{133}Cs^+$ primary ion beam with a 20 kV total accelerating voltage was used. A carbon coat of ~25 nm thickness was applied on the sample surface and a normal incidence electron gun was used for charge compensation of the sample surface. The accelerating voltage of secondary ions was 10 kV.

As a result of the small grain size (typically <10 μm in size) of minerals in samples, a small $^{133}Cs^+$ primary beam (~3 μm, ~25 pA) was mainly used for oxygen three-isotope analyses of forsterite, melilite, spinel, anorthite, and Al-Ti-rich diopside within the interior of refractory inclusions and their rims. Secondary ions of oxygen isotopes were simultaneously detected, using one Faraday cup (FC) for $^{16}O^-$ and two electron multipliers (EM) for $^{17}O^-$ and $^{18}O^-$, respectively. The mass resolving power (MRP at 10% peak height) was set to ~2200 for $^{16}O^-$ and $^{18}O^-$, and ~6000 for $^{17}O^-$, respectively. The typical count rate of $^{16}O^-$ was 2.3×10^7 cps. These analytical conditions are similar to those described in Nakamura et al. (2008) and Ushikubo et al. (2012).

For larger grains, a higher-intensity $^{133}Cs^+$ primary beam (~15 µm, ~3 nA) was used for oxygen three-isotope analyses of several forsterites and Al-Ti-rich diopsides in AOAs. In this configuration, secondary ions of oxygen isotopes were simultaneously measured with three FC detectors, using a 10^{10} ohm resistor for $^{16}O^-$ and 10^{11} ohm resistors for $^{17}O^-$ and $^{18}O^-$, respectively. The mass resolving power (MRP at 10% peak height) was set to ~2200 for $^{16}O^-$ and $^{18}O^-$, and ~5000 for $^{17}O^-$, respectively. The typical count rate of $^{16}O^-$ was 2.7×10^9 cps. These analytical conditions are similar to those described in Kita et al. (2010) and Ushikubo et al. (2012).

For small and large spot analyses, the count rate of $^{16}OH^-$ was measured immediately after each oxygen isotope analysis. The contribution of $^{16}OH^-$ to $^{17}O^-$ was estimated following methods developed by Heck et al., (2010), and was typically found to be <0.1‰.

A San Carlos olivine standard ($\delta^{18}O_{VSMOW}$=5.32‰, Kita et al., 2010) was used as the running standard. The instrumental bias effect on $\delta^{18}O$ (i.e. the matrix effect) was calibrated based on analyses of multiple standards (Fo_{100} and Fo_{89} for olivine, synthetic gehlenite and åkermanite for melilite, diopside and synthetic Al-Ti-rich diopsidic glass for pyroxene, spinel, and anorthite, Tables EA1 and EA3). No apparent matrix effect on $\Delta^{17}O$ was observed (Table EA3). Procedures for the instrumental bias correction and for data reduction are described in Kita et al. (2009) and Tenner et al. (2013). The external reproducibilities of bracketing standard analyses were assigned as the uncertainty of unknown samples. Typical uncertainties (2 SD) of $\delta^{18}O$, $\delta^{17}O$, and $\Delta^{17}O$ were ±1.1‰, ±1.1‰, and ±1.1‰, respectively, with the small beam analytical setting, and ±0.26‰, ±0.61‰, and ±0.59‰, respectively, with the large beam analytical setting.

3.2.2 ^{26}Al-^{26}Mg isotope systematics

For analysis of Al and Mg isotopes, an $^{16}O^-$ primary beam with a 23 kV total accelerating voltage was used. A ~25 nm thick carbon coat was applied on the sample surface. The accelerating voltage of secondary ions was 10 kV.

A small $^{16}O^-$ primary beam (5 to 7 µm, 40 to 150 pA) was used for analyses of anorthite and melilite. Secondary ions of $^{24}Mg^+$, $^{25}Mg^+$, and $^{26}Mg^+$ were detected by an axial EM detector that operated by magnetic peak switching. Secondary $^{27}Al^+$ ions were detected by a Faraday cup located at the high mass side of the axial EM detector during the measurement of $^{25}Mg^+$. The mass resolving power was set at ~4000, which is sufficient for the separating $^{48}Ca^{2+}$ and $^{24}MgH^+$ interferences. Dead time of the EM detector was 24.9 ns, as determined by Mg isotope analyses of melilite and anorthite standards. This analytical protocol is similar to that described in Ushikubo et al. (2013).

For small beam analyses, synthetic glass standards (Åk15 and anorthitic glass with 1wt% MgO) were used to determine respective instrumental mass biases (Table EA4). The procedures to calculate the mass-dependent fractionation ($\delta^{25}Mg_{DSM3}$) and the ^{26}Mg-excess ($\delta^{26}Mg^*$) are provided in Electronic Annex (EA-1). The $\delta^{25}Mg_{DSM3}$ uncertainty of melilite unknowns is assigned as $\{(2SE_{internal})^2+(2SE_{std})^2\}^{1/2}$. The uncertainties of the $\delta^{25}Mg_{DSM3}$ value of anorthite and the $\delta^{26}Mg^*$ values of melilite and anorthite are assigned as the internal 2SE ($2SE_{internal}$) of each analysis because statistical uncertainties based on total counts of signals are significantly larger than reproducibilities of spot-to-spot analyses (Table 2 and Table EA4 for $\delta^{26}Mg^*$ values of melilite, Table 2, and Table S2 in Ushikubo et al., 2013 for $\delta^{25}Mg_{DSM3}$ and $\delta^{26}Mg^*$ values of anorthite, respectively).

For larger phenocrysts consisting of forsterite, spinel, and Al-Ti-rich diopside, a higher-intensity $^{16}O^-$ primary beam (~10 μm, 2.2 nA) was employed. Secondary ions of $^{24}Mg^+$, $^{25}Mg^+$, $^{26}Mg^+$, and $^{27}Al^+$ were simultaneously detected by four Faraday cups. The mass resolving power was set at ~2200 and the tailing of interference peaks was negligibly small. Overall, this condition is similar to that described in Kita et al. (2012) and Ushikubo et al. (2013).

For large beam analyses, a San Carlos olivine standard ($\delta^{25}Mg_{DSM3}$=−0.02‰) was used as the running standard. The $\delta^{25}Mg_{DSM3}$ matrix effect was calibrated based on analyses of multiple standards (Fo_{100} and San Carlos olivine (Fo_{89}) for olivine, diopside and synthetic Al-Ti-rich diopsidic glass for pyroxene, and spinel, Table EA4). The procedure to calculate the mass-dependent fractionation ($\delta^{25}Mg_{DSM3}$) and ^{26}Mg-excess ($\delta^{26}Mg^*$) is provided in Electronic Annex (EA-1). The external reproducibility of bracketing standard analyses (2SD) is assigned as the uncertainty of unknown samples. Typical uncertainties of $\delta^{25}Mg_{DSM3}$ and $\delta^{26}Mg^*$ were ±0.19‰ and ±0.11‰, respectively.

The relative sensitivity factors (RSF, $(^{27}Al/^{24}Mg)/(^{27}Al^+/^{24}Mg^+)$) of spinel, Al-Ti-rich diopside, melilite, and anorthite were determined based on EPMA data and results of standard analyses by SIMS (Table EA4).

4. Results

Representative major element compositions of individual phases and analysis positions from samples by EPMA are summarized in Table EA2 and Figure EA1. Oxygen three-isotope data and Mg isotope data are summarized in Table 1 and Table 2, respectively. Locations of individual analyses within refractory inclusions are shown in Figure EA2. All individual data, including analyses of running standards, are shown in Table EA5-8.

4.1. Oxygen isotope ratios

Oxygen isotope ratios of all measured samples are significantly ^{16}O-rich ($\Delta^{17}O<-20‰$) and are distributed near the CCAM line (Table 1, Fig. 4). For a given refractory inclusion, the $\Delta^{17}O$ values of all measured phases are consistent within analytical uncertainty; the only exception is a relatively ^{16}O-poor datum from a thin melilite layer at the rim of Y81020-E-8 ($\Delta^{17}O=-14.3\pm0.5‰$, Fig. 4a). No detectable systematic differences in both $\delta^{18}O$ and $\Delta^{17}O$ are observed between oxygen isotope ratios of minerals in the interior and those of minerals in the rim (i.e. Ti, Al-bearing diopside and spinel in CAIs and olivine at the edge of AOAs) (Table 1, Figs. 4 and 5). Subtle variation of oxygen isotope ratios along a slope 1 line within each inclusion (e.g., AOA G58, Fig.4k) are recognized. However, these differences are small when considering the analytical uncertainty. Averaged $\Delta^{17}O$ of the CAIs and AOAs studied have values of −22.0 to −24.3‰, and have uncertainty ranging from 0.3‰ to 0.9‰ (Table 1).

4.2. Magnesium isotope ratios and the ^{26}Al-^{26}Mg isotope systematics

Magnesium isotope ratios ($\delta^{25}Mg_{DSM3}$ and $\delta^{26}Mg^*$), $^{27}Al/^{24}Mg$ ratios, and the regression lines of the Al-Mg isotope systematics are summarized in Table 2. The ^{26}Al-^{26}Mg isotope systematics of all melilite-rich CAIs (Y81020-E-8, G5, G16, G49, and G104) exhibit single linear correlations in $\delta^{26}Mg^*$ vs. $^{27}Al/^{24}Mg$ (Figs. 6a-f). The $^{27}Al/^{24}Mg$ ratios of melilite-rich CAIs are highly variable (from 10 to 72). Melilite in CAI G5 is highly gehlenitic (Al-rich, $^{27}Al/^{24}Mg$= 46 to 72) and in CAI G49 it is åkermanitic (Mg-rich, $^{27}Al/^{24}Mg$= 10 to 18) relative to other melilite-rich CAIs ($^{27}Al/^{24}Mg$= 15 to 37). Anorthite in CAI G16 has a very high $^{27}Al/^{24}Mg$ ratio and a large ^{26}Mg-excess (~1560 and ~530‰, respectively, Table 2). The inferred initial $^{26}Al/^{27}Al$ ratios, $(^{26}Al/^{27}Al)_0$, of melilite-rich CAIs are $(4.08\pm0.75)\times10^{-5}$ to $(5.05\pm0.18)\times10^{-5}$. These values are within the $(^{26}Al/^{27}Al)_0$ range of CAIs from CV chondrites but are slightly lower than the canonical Solar System value of $(5.25\pm0.02)\times10^{-5}$ (e.g., Jacobsen et al., 2008; Larsen et al., 2011; MacPherson et al., 2012; Kita et al., 2013). One AOA, G17, has an inferred $(^{26}Al/^{27}Al)_0$ of $(5.32\pm0.81)\times10^{-5}$, which is based on data from olivine, Al-Ti-rich diopside, and spinel (Fig. 6i). The other three AOAs, G28, G44, and G58, do not contain high-Al/Mg phases that are large enough for Mg isotope analyses by SIMS.

Regarding the ^{26}Al-^{26}Mg isotope systematics of anorthite-rich CAI G92, two distinct trend lines are produced when plotting ^{27}Al/^{24}Mg vs. ^{26}Mg-excess (δ^{26}Mg*) (Figs. 6g, 6h). In particular, melilite and Al-Ti-rich diopside data of CAI G92 are distributed along a single trend line. The slope of the trend line using only Al-Ti-rich diopside data is 0.33±0.19 with intercept of 0.18±0.17, which overlaps with the melilite data. The slope of the trend line using both Al-Ti-rich diopside and melilite data is 0.375±0.14, corresponding to an inferred (^{26}Al/^{27}Al)$_0$ of (5.2±2.0)×10^{-5} (Fig. 6g). Although we cannot determine the origin of Al-Ti-rich diopside with certainty, a consistent distribution of Al-Ti-rich diopside and melilite data suggests these are primary phases. In contrast, anorthite data from G92 exhibit high ^{27}Al/^{24}Mg (>700) and ^{26}Mg-excesses that are significantly smaller than those from the regression line of melilite and Al-Ti-rich diopside data (Fig. 6h). Assuming that anorthite formed by replacing melilite and that Mg within anorthite had originally derived from the melilite that it replaced (see discussion in section 5.2), the regression line using data from melilite and anorthite in G92 has a slope of 0.0374±0.0039 with an intercept of 2.6±1.1‰ and an inferred (^{26}Al/^{27}Al)$_0$ of (5.21±0.54)×10^{-6} (Fig. 6h, Table 2). We note that the inferred (^{26}Al/^{27}Al)$_0$ becomes slightly reduced [(4.6±2.1)×10^{-6}] using only anorthite data and it is slightly higher [(5.59±0.53)×10^{-6}] if assuming no ^{26}Mg-excess when anorthite formed.

In addition to CAI G92, anorthite is also observed in melilite-rich CAI, G16, occurring as a thin layer (~5 μm) between melilite and the diopside rim (Fig. 1g). However, anorthite in CAI G16 has a large ^{26}Mg-excess which is consistent with the regression line of coexisting Al-Ti-rich diopside and melilite that corresponds to a (^{26}Al/^{27}Al)$_0$ of (4.71±0.15)×10^{-5} (Fig. 6d, e). Thus, anorthite grains from two different CAIs, G92 and G16, record distinct ^{26}Al-^{26}Mg isotope signatures within the same thin section.

High precision Mg isotope data of Mg-rich phases (olivine, Al-Ti-rich diopside, and spinel) obtained by large beam analyses indicate that mass-dependent Mg isotope fractionation (δ^{25}Mg$_{DSM3}$) is small (0.0±1.5‰/amu, Table 2). This result is consistent with the fine-grained textures and/or irregular shapes of the samples, which suggests they avoided re-melting and associated evaporative loss to the surrounding environment. A few δ^{25}Mg$_{DSM3}$ values of high-^{27}Al/^{24}Mg phases (melilite and anorthite) that were obtained by small beam analyses are significantly higher than other data in the same inclusion, beyond the analytical uncertainty (e.g., #53 of G5, #50 of G49, and #37 of G92 in Table 2). These are presumably outliers of small beam analyses, but we cannot completely rule out the existence of δ^{25}Mg$_{DSM3}$ heterogeneity within each inclusion.

5. Discussion

5.1. ^{16}O-enriched environment of refractory inclusion formation

Within a given inclusion, oxygen isotope ratios of its rim structures, including diopside and spinel in CAIs, as well as olivine at the edge of AOAs, can be compared to those of interior phases, in order to determine which oxygen isotope reservoirs were sampled. With the exception of one datum (discussed below), our results indicate that oxygen isotope ratios of minerals both in the rim and in the interior of the same inclusion are indistinguishable, and show no systematic differences (Figs. 4 and 5). This result is distinct from variable oxygen isotope ratios of Wark-Lovering rims associated with coarse-grained CAIs from CV chondrites (e.g., Yoshitake et al., 2005; Simon et al., 2011, 2016), but in agreement with oxygen isotope ratios of CAIs from pristine CR, CO, and CH chondrites (Bodénan et al., 2014; Jacobsen et al., 2014; Krot et al., 2016).

The single, relatively ^{16}O-poor signature (Δ^{17}O~−14‰) of melilite outside of the rim spinel layer of CAI Y81020-E-8 (Fig. 1e and 4b) can be interpreted in a couple ways. For example, it could be an intrinsic signature (condensation from a relatively ^{16}O-depleted nebular gas) or it could be the result of later metamorphism. The analyzed region of this melilite is surrounded by fine-scale cracks and voids and directly contacts with the matrix, as the diopside layer in this CAI is discontinuous (Fig. EA2, Y81020-E-8_2). Considering the susceptibility of oxygen isotope disturbance within melilite (e.g., Fagan et al., 2004; Bodénan et al., 2014), while also taking into account the consistent ^{16}O-rich signature of other CAI rim phases from the least metamorphosed carbonaceous chondrites (e.g., Bodénan et al., 2014; Jacobsen et al., 2014; Krot et al., 2016; this study), the relatively ^{16}O-poor signature of melilite outside of the rim spinel layer of Y81020-E-8 is probably the result of later isotopic exchange, either in the solar nebula or in the parent body.

CAIs from this study have a small but appreciable range in averaged Δ^{17}O values, on the order of a few per-mil when considering uncertainties (Table 1, Fig. 4, 5, and 8a). With the exception of the outermost melilite layer of Y81020-E-8, as discussed in the previous paragraph, oxygen isotope ratios of CAI rims are within the range of those from their corresponding interior phases (e.g., Table 1 and Figs. 4 and 5). This indicates that both of these CAI components formed in the same oxygen isotope environment and that their intrinsic oxygen isotope ratios have not been disturbed after their formation. Considering the pristine nature of Acfer 094 and Y-81020 chondrites, the slight Δ^{17}O variation in their CAIs most likely reflects that of the oxygen isotope environment where CAIs formed. Similar, as well as slightly larger Δ^{17}O variations along the PCM line are also found in hibonite and spinel-hibonite inclusions from CM chondrites (Kööp et al., 2016). Although extremely ^{16}O-rich inclusions (Δ^{17}O down to

~−37‰, Kobayashi et al., 2003; Gounelle et al., 2009, see also Fig. EA1-2 in Ushikubo et al., 2012 for comparison) have been found, we do not recognize such an extremely ^{16}O-rich signature in the samples, suggesting either the occurrence of extremely ^{16}O-rich environment or formation of inclusions in an extremely ^{16}O-rich environment was rare.

Regarding the origin of CAI rims, it has been proposed that Wark-Lovering rims formed by a later flash heating event, leading to intense evaporative loss (e.g., Wark and Boynton, 2001). Such a process is considered to be responsible for positive mass-dependent isotope fractionation that is commonly observed in F(UN) inclusions and normal CAIs (e.g., Clayton and Mayeda, 1977; Wasserburg et al., 1977; Grossman et al., 2008; Krot et al., 2014a). Although the samples from this study are mainly fine-grained CAIs, they have similar textures (i.e. thin spinel and diopside layered structures) as those observed in Work-Lovering rims. However, the rim δ^{18}O values (Table 1, Fig. 5b) and $\delta^{25}\mathrm{Mg}_{\mathrm{DSM3}}$ values (Table 2) from Acfer 094 and Y-81020 refractory inclusions exhibit neither mass-dependent isotope fractionation nor variability in Δ^{17}O. These data indicate that later processes, such as an intense flash re-heating event, are not necessary to produce the rim structure of CAIs. In addition, similar ^{16}O-rich oxygen isotopic signatures, as well as general agreement of oxygen isotope ratios between CAI interior phases and their rims (including fine-grained CAIs and coarse-grained Wark-Lovering rim-bearing CAIs) are consistently observed in CAIs from pristine carbonaceous chondrites (Bodénan et al., 2014; Jacobsen et al., 2014; Krot et al., 2016; this study). Combined these results indicate that all components and textures of CAIs, including condensation of refractory phases from nebular gas, aggregation, and formation of rim layers, occurred in the same ^{16}O-rich environment. The observed oxygen isotope variability among Wark-Lovering rims of coarse-grained CV chondrite CAIs is probably explained by oxygen isotope exchange with ^{16}O-poor materials during parent body metamorphism.

5.2. Δ^{17}O vs. $(^{26}\mathrm{Al}/^{27}\mathrm{Al})_0$ of CAIs: An enigmatic anorthite-rich CAI having low $(^{26}\mathrm{Al}/^{27}\mathrm{Al})_0$ and an ^{16}O-rich signature.

Figure 7 summarizes the relationship between Δ^{17}O and $(^{26}\mathrm{Al}/^{27}\mathrm{Al})_0$ of the refractory inclusions in this study; data from Acfer 094 chondrules (Ushikubo et al., 2013) are also shown for comparison. Inferred $(^{26}\mathrm{Al}/^{27}\mathrm{Al})_0$ values of CAIs Y81020-E-8, G5, G16, G49, and G104 range from $(4.08\pm0.75)\times10^{-5}$ to $(5.05\pm0.18)\times10^{-5}$, which are slightly lower than the canonical value of $(5.25\pm0.02)\times10^{-5}$ (Fig. 7). These values are similar to those of melted CAIs from CV and CR chondrites (Makide et al., 2009; MacPherson et al., 2012). As CAIs Y81020-E-8, G5, G16, G49, and G104 have well-defined isochrons, and because they have primitive textures, such as small grain sizes and multi-nodule structures, they likely did not experience a later re-melting process. Assuming this is true, and also assuming homogeneously distributed ^{26}Al after "canonical" CAIs formed (e.g., Kita et al., 2013), their slightly lower $(^{26}\mathrm{Al}/^{27}\mathrm{Al})_0$ values indicate formation up to ~0.3 Ma after canonical CAIs (Fig. 7). However, it cannot be ruled out that these fine-grained CAIs formed prior to homogeneous distribution of ^{26}Al and that the range of $(^{26}\mathrm{Al}/^{27}\mathrm{Al})_0$ values among Acfer 094 and Y-81020 refractory inclusions represents variability of ^{26}Al abundance in the early solar system when they formed. For AOA G17, the inferred $(^{26}\mathrm{Al}/^{27}\mathrm{Al})_0$ value of $(5.32\pm0.81)\times10^{-5}$ is consistent with the canonical value of CAIs. As such, this AOA could be as old as other CAIs although the present data are not of sufficient precision to discuss fine-scale differences of formation ages. Regarding oxygen isotope ratios, all of the aforementioned CAIs, as well as AOA G17, are ^{16}O-rich, likely reflecting the value of the nebular gas over this time period.

CAI G92 is also ^{16}O-rich, but its constituent anorthite has an order-of-magnitude lower inferred $(^{26}\mathrm{Al}/^{27}\mathrm{Al})_0$, $(5.21\pm0.54)\times10^{-6}$, when compared to the CAIs and the AOA mentioned above (Fig. 7). However, there is also another trend line corresponding to a $(^{26}\mathrm{Al}/^{27}\mathrm{Al})_0$ of $(5.2\pm2.0)\times10^{-5}$ that is observed among Al-Ti-rich diopside and melilite in CAI G92 (Fig. 6g, Table 2), making it evident that this CAI initially had a near-canonical $(^{26}\mathrm{Al}/^{27}\mathrm{Al})_0$, like the other refractory inclusions. A later isotopic disturbance in the Acfer 094 parent body is unlikely to explain the lower $\delta^{26}\mathrm{Mg}^*$ values in G92 anorthite because (1) as mentioned in the Introduction, Acfer 094 is one of the least metamorphosed carbonaceous chondrites (Greshake, 1997; Kimura et al., 2008) and (2) the ^{26}Al-^{26}Mg systematics of both the anorthite rim layer in CAI G16 (Fig. 6e) and small anorthite grains in chondrules from the same thin section do not exhibit evidence for isotopic disturbance (this study, Kita et al., 2013; Ushikubo et al., 2013). As such, we interpret that the lower $(^{26}\mathrm{Al}/^{27}\mathrm{Al})_0$ of G92 anorthite (Fig. 6h) recorded the timing of a later thermal process in the solar nebula.

Like anorthite in CAI G92, Krot et al. (2014b) reported that anorthite in some AOAs from CH chondrites have similar ^{16}O-rich oxygen isotope ratios but low $\delta^{26}\mathrm{Mg}^*$ values. They proposed that such an isotopic signature in anorthite could be explained by Mg isotopic exchange with surrounding Mg-rich phases during a days-to-weeks long thermal annealing event at high temperature (~1100°C) coupled with a slow cooling rate (~0.01 K/h). Such conditions would be necessary because the diffusivity of Mg in anorthite is significantly higher than that of oxygen at >1000 °C. However, such a scenario is unlikely for G92 because a linear correlation between $^{27}\mathrm{Al}/^{24}\mathrm{Mg}$ ratios and $\delta^{26}\mathrm{Mg}^*$ values in anorthite is not consistent with a later isotopic disturbance of the ^{27}Al-

^{24}Mg systematics in anorthite (e.g., Podosek et al, 1991; MacPherson et al., 2012). Further, the near-canonical isochron produced by Al-Ti-rich diopside and melilite in G92 (Fig. 6g) is not consistent with Mg isotopic exchange with adjacent anorthite. If anorthite in G92 formed as early as other phases, the accumulated ^{26}Mg-excess would have been larger than 300‰ in δ^{26}Mg* (e.g., anorthite in CAI G16, Fig. 6e) at the time of the thermal annealing event. Thus, even though Mg is a minor element in anorthite (<0.1wt%), anomalously high δ^{26}Mg* values (up to a few permil) in Mg-rich phases are expected to be observed if Mg isotopic exchange occurred (e.g., Podosek et al., 1991; MacPherson et al., 2012). Moreover, contrary to typical AOAs, anorthite in G92 is the predominant phase and is not always associated with spinel, meaning that complete resetting of the anorthite ^{26}Al-^{26}Mg systematics by isotopic exchange with Mg-rich phases would probably take much longer. In contrast, exchange with an ^{16}O-poor ambient gas would have effectively occurred because of the fine-grained texture in this CAI.

As an alternative to the low excess-^{26}Mg in G92 anorthite being due to solid-state exchange-induced resetting, a more likely possibility is that G92 originally formed as a fine-grained melilite-rich CAI, and that the anorthite replaced the melilite after most of the ^{26}Al decayed. This idea presupposes that the occurrence of low δ^{26}Mg* in anorthite-rich CAI G92 is not a coincidence, but is instead the result of later high temperature process in the solar nebula. Replacement of melilite by anorthite could have occurred by interaction with the ambient gas: $Ca_2Al_2SiO_7$ (Gehlenite) + $3SiO(g) + Mg(g) + 4H_2O(g) \rightarrow CaAl_2Si_2O_8$ (anorthite) + $CaMgSi_2O_6$ (diopside) + $4H_2(g)$ (Krot et al., 2004b), or under an oxidizing environment, as the following reaction: $Ca_2Al_2SiO_7 + SiO(g) + H_2O(g) + CO_2(g) \rightarrow CaAl_2Si_2O_8 + Ca(OH)_2(g) + CO(g)$ is also proposed (Hashimoto, 1992). Even though spinel ($MgAl_2O_4$) and åkermanite ($Ca_2MgSi_2O_7$) could have partly contributed Mg and Si to produce diopside in these reactions, replacement of melilite requires incorporation of SiO from outside of the CAI. As such, the oxygen isotope ratio of anorthite produced by reaction must have been affected by the oxygen isotope ratio of an ambient gas. Assuming the composition of the initial melilite of CAI G92 was the same as that of remaining melilite ($Åk_{20}$), and that Mg was completely consumed to form diopside by replacement of melilite, abundant diopside (~20 molar% of anorthite, assuming gehlenite : åkermanite = anorthite : diopside = 4 : 1) would have formed with anorthite. Since sub-μm high-Ca pyroxene inclusions in anorthite and small and irregular-shaped Al-Ti-rich diopside grains are abundant in the interior of CAI G92 (Fig. 2b), they may have formed by replacement of melilite. However, due to the limitation of analysis spot size by SIMS (~3μm in size for O isotope analyses and ~10μm for Mg isotope analyses of Mg-rich phases), we could not perform isotope analyses of sub-μm diopside inclusions, nor could we analyze the outermost margin of diopside, in order to investigate if their characteristics were established during the replacement of melilite. With regard to anorthite, very low Mg concentrations of anorthite in G92, as well as those of the thin anorthite layer in G16 (^{27}Al/^{24}Mg=700 to 1560, 0.03 to 0.015wt.% MgO), suggest that the formation process of anorthite in these CAIs was different than that of igneous anorthite in type B CAIs (typically ^{27}Al/^{24}Mg=100 to 600, 0.23 to 0.04wt.%, e.g., Podosek et al., 1991; Goswami et al., 1994; Makide et al., 2009; Kita et al., 2012). In addition, the absence of anomalously high δ^{26}Mg* among G92 Mg-rich phases is consistent with the replacement of melilite by anorthite, after most ^{26}Al had decayed. If G92 anorthite initially formed with the canonical abundance of the short-lived nuclide ^{26}Al, followed by later Mg isotopic exchange, an occurrence of anomalously high δ^{26}Mg* (i.e. above the canonical isochron) would be expected in Mg-rich phases such as spinel, Al-Ti-rich diopside, and melilite (e.g., Podosek et al., 1991; MacPherson et al., 2012). Instead, if anorthite formed by replacing primary melilite after the decay of most ^{26}Al, it might have inherited the ^{26}Mg-excess of precursor melilite (e.g., δ^{26}Mg*: ~3‰, Figs. 6g and 6h). In this case, the slope of the regression line using anorthite and melilite data represents the (^{26}Al/^{27}Al)$_0$ when anorthite formed. Another possibility is that G92 anorthite had no ^{26}Mg-excess when it initially formed, because it incorporated Mg from the ambient gas. If this is the case, the regression line through the origin using anorthite data would be appropriate, as well as its corresponding inferred (^{26}Al/^{27}Al)$_0$, ~5.5×10^{-6}, which is slightly higher than the inferred (^{26}Al/^{27}Al)$_0$ of 5.21×10^{-6} when using anorthite and melilite data. Here we assume that Al was absent from the ambient nebular gas because of its highly refractory nature (e.g., Lodders, 2003). Regardless of whether or not G92 anorthite initially inherited ^{26}Mg-excess from melilite, ^{26}Al would have been supplied from the reacted primary melilite. Assuming this formation mechanism is correct, the ^{26}Al-^{26}Mg systematics of G92 anorthite and melilite, whose data are distributed along a single regression line (MSWD=0.95, Fig. 6h), can be used to deduce the time interval between the CAI formation and the later formation of anorthite.

The inferred (^{26}Al/^{27}Al)$_0$, $(5.21\pm0.54)\times10^{-6}$, of G92 anorthite indicates formation 2.3 Ma after CAIs (Fig. 7). This result coincides with the timing of chondrule formation among ordinary and carbonaceous chondrites (e.g., Kita and Ushikubo, 2012; Ushikubo et al., 2013). As similar ages are also observed in CAI-chondrule compound objects in CR chondrites ((^{26}Al/^{27}Al)$_0$ of $<2\times10^{-6}$ to $(3.8\pm1.3)\times10^{-6}$, Makide et al., 2009), energetic events in the solar nebula that imposed igneous and metamorphic processes among CAIs and chondrules are inferred to have occurred at 2 – 3 Ma after canonical CAI formation. Regarding chondrule formation, it is inferred that the environment was ^{16}O-poor relative to the environment where refractory inclusions formed, as oxygen isotope ratios of chondrules are typically $\Delta^{17}O$=−6 to 2‰ (Connolly and Huss, 2010; Kita et al., 2010; Krot et al., 2010b; Rudraswami et al., 2011; Weisberg et al., 2011; Nakashima et al., 2012; Ushikubo et al., 2012; Schrader et al., 2013, 2014; Tenner et al., 2013, 2015). This inference is also supported by characteristics of CAI-chondrule compound objects, as their ^{16}O-rich CAI-like domains are enclosed by ^{16}O-poor ferromagnesian minerals (Makide et al., 2009). In contrast, CAI G92 does not contain ^{16}O-poor ferromagnesian phases (olivine and low-Ca pyroxene) or Fe-Ni metal (Fig. 2b). Thus, even though G92 anorthite has a similar inferred $(^{26}Al/^{27}Al)_0$ as chondrules, it differs from chondrules and CAI-chondrule compound objects. Combined, these characteristics of CAI G92 indicate the existence of an ^{16}O-rich environment ($\Delta^{17}O$~−23‰, Figs. 4g and 7) that was devoid of ^{16}O-poor ferromagnesian dust, approximately 2 – 3 Ma after CAI formation.

A conceivable scenario is that G92 anorthite formed at the inner edge of the solar nebula, where ambient gas may still have been ^{16}O-rich 2 – 3 Ma after CAI formations (possibly because this region is close to the Sun, the predominant reservoir of ^{16}O-rich solar gas). Then, following the formation of anorthite, CAI G92 could have been transferred to the outer asteroid belt. However, this scenario seems unlikely because (1) it would have been difficult to avoid any reprocessing until ~2 Ma after CAIs if G92 remained close to the Sun over that time interval; and (2) outward mass transport was likely insufficient ~2 Ma after CAIs (Ciesla, 2010; Jacquet, 2013).

Alternatively, a more plausible scenario is that G92 anorthite formed at a large vertical distance relative to the chondrule-forming mid-plane of the protoplanetary disk. Here, it is assumed (1) an ^{16}O-rich gas would have been a major oxygen isotopic component, because it has been ubiquitously present throughout the history of the Solar System; and (2) the mid-plane of the protoplanetary disk was dominated by ^{16}O-poor silicate dust (e.g., Tenner et al., 2015) and early Solar System H_2O ice (e.g., Sakamoto et al., 2007), particularly after cooling of the solar nebula and with reduced turbulent flow. The former assumption is possible when considering that the present solar wind is ^{16}O-rich ($\Delta^{17}O$=−28.4±1.8‰, McKeegan et al., 2011). The latter is valid because high dust to gas ratios (e.g. Ebel and Grossman, 2000; Alexander 2004), as well as enhancement of H_2O ice (e.g., Fedkin and Grossman, 2006; 2016), were likely necessary to create an environment oxidized enough to form the chondrule assemblage. The settling of ^{16}O-poor H_2O ice and dust toward the mid-plane of the protoplanetary disk would have caused a vertical oxygen isotopic gradient in the protoplanetary disk (e.g., Yurimoto et al., 2007) at the time of chondrule formations. Under such an environment, products of high-temperature processes would have different oxygen isotope ratios as a function of their vertical distance from the mid-plane. For example, Tenner et al. (2015) demonstrated that variable additions of ^{16}O-poor dust and H_2O ice ($\Delta^{17}O \sim -6‰$ and +5‰, respectively) to ^{16}O-rich gas ($\Delta^{17}O \sim -28.4‰$) can explain the observed $\Delta^{17}O$ – Mg# trend among ferromagnesian silicates in carbonaceous chondrite chondrules. As such, materials that formed vertically far from the mid-plane could have been enriched in ^{16}O, because such a region would have been depleted in ^{16}O-poor dust and H_2O ice, and therefore would have been dominated by ^{16}O-rich gas. We note that large silicate particles like CAI G92 (a few hundred μm in size) must have been rare at a vertically distant place from the mid-plane after the settling of dusts to the mid-plane (e.g., Ciesla, 2009; Jacquet, 2013). It is more favorable that much smaller refractory inclusions would prevail at large vertical distance from the mid-plane. As such, small refractory inclusion may have a higher likelihood of showing evidence for re-heating events in an ^{16}O-rich environment.

Considering the prevalence of chondrules in unequilibrated chondrites (20-80 volume percent; Scott et al., 1996), it is evident that one or more pervasive processes produced silicate melts ~2 Ma after CAIs, and several mechanisms that have been proposed for their formation (see Ciesla, 2005; Desch et al., 2012 for review). Assuming the energy source of G92 anorthite formation was similar to that which formed chondrules, a vertically distant location from the mid-plane of the protoplanetary disk seems a more appropriate site than the inner edge of the solar nebula to explain both a younger anorthite formation age (~2 Ma after CAIs) and the lack of accumulated ferromagnesian phases.

5.3. ^{16}O-rich dust component and correlation lines

Fine-grained CAIs and AOAs formed by aggregation of primary condensates from early solar nebular gas, and they avoided re-melting by a later heating event in the solar nebula. The limited range of $\delta^{25}Mg_{DSM3}$ values among the fine-grained refractory inclusions studied (−0.4 to 1.3‰) supports this idea. Thus, we suggest that fine-grained CAIs and AOAs from type 3.00-3.05 chondrites are the best candidates for recording pristine oxygen isotope ratios of early solar system condensates.

Figure 8 shows averaged oxygen isotope ratios of individual refractory inclusions (Fig.8a), as well as those from AOA forsterite and Al-Ti-rich diopside (Fig.8b, see also Table 2) obtained using a high intensity primary beam (small beam data are only used to calculate averaged values of individual samples, due to their large uncertainties). The oxygen isotope ratios of fine-grained Acfer 094 and Y-81020 refractory inclusions are tightly distributed between the CCAM line (Clayton et al., 1977) and the PCM regression line defined based on olivine and low-Ca pyroxene data from

Acfer 094 chondrules (Ushikubo et al., 2012). Deviations in averaged $\delta^{18}O$ values from the CCAM line, relative to the mass-dependent isotope fractionation trend ($\delta^{17}O=0.52\times\delta^{18}O$), range from −0.6‰ (CAI G16) to +1.9‰ (CAI G5), with an average value of +0.6‰. These results indicate that oxygen isotope ratios of pristine CAI precursor dusts were distributed along the CCAM line, or, at most, were ~1‰ to the right of the CCAM line. Note that we cannot precisely determine the oxygen isotope ratio of the primordial nebular gas from fine-grained refractory inclusion data because the degree of equilibrium oxygen isotope fractionation between gas and dust can vary as a function of temperature and gas composition (e.g., $\delta^{18}O$ value of olivine could be 2 to 3‰ lighter than that of ambient gas, Clayton et al., 1991; Kita et al., 2010). Regarding the PCM line (Ushikubo et al., 2012) and its uncertainty (~±0.7‰), it is indistinguishable from the Acfer 094 and Y-81020 refractory inclusion data. This is an important consideration for two reasons. First, it indicates that Acfer 094 chondrules and refractory inclusions represent a consistent mixing line of early Solar System materials. Second, and with respect to relict olivine grains in Acfer 094 chondrules, the most ^{16}O-rich examples have oxygen isotope ratio that are indistinguishable from Acfer 094 refractory inclusion data (Fig. 9). This overlap is consistent with the idea that ^{16}O-rich relict olivine derived from refractory inclusion related material (e.g., AOA, olivine in the accretionary rim of CAIs).

Beyond linking Acfer 094 chondrules and refractory inclusions together, the PCM line carries with it other important characteristics. For example, oxygen isotope data from extremely ^{16}O-poor Acfer 094 cosmic symplectites (Sakamoto et al., 2007; Seto et al., 2008) plot on the PCM line (Fig. 9). The PCM line also intersects with the terrestrial fractionation (TF) line at $\delta^{18}O=5.8\pm0.4$‰ (Ushikubo et al., 2012), which is in agreement with the terrestrial mantle value ($\delta^{18}O=5.5\pm0.2$‰; Eiler, 2001). Taking all of these things into consideration, it is apparent that most primary materials from carbonaceous chondrites experienced very little mass-dependent oxygen isotope fractionation. Further, if all of the aforementioned materials within Acfer 094 are indeed related, it suggests that ^{16}O-rich nebular gas and ^{16}O-poor (or $^{17,18}O$-rich) primordial volatiles represent endmembers of a linear trend (i.e., the PCM line) with a mass-independent fractionated slope of ~1.0.

6. Conclusions

Oxygen isotope ratios and ^{26}Al-^{26}Mg isotope systematics of multiple phases in refractory inclusions (5 spinel-melilite-rich CAIs, 1 pyroxene-anorthite-rich CAI, and 4 AOAs) from the least metamorphosed carbonaceous chondrites, Acfer 094 (C-ungrouped 3.00) and Y-81020 (CO3.05), were investigated.

All samples have ^{16}O-rich signatures but exhibit subtle and detectable variabilities in oxygen isotope ratios among individual refractory inclusions (Δ^{17}O=−22.0±0.5‰ to −24.3±0.3‰). This indicates slight oxygen isotope variations of early solar nebular gas where refractory inclusions formed.

Within analytical uncertainties, oxygen isotope ratios of rim spinel and diopside match those of interior phases in each CAI. In addition, no apparent mass-dependent isotopic fractionation is observed in O and Mg isotope ratios of rim phases. These observations do not agree with flash heating and evaporative loss of relatively volatile elements during rim formation. Instead, our results suggest that condensation and aggregation of interior phases, as well as the formation of CAI rim structures, occurred in the same environment.

Inferred initial ^{26}Al/^{27}Al ratios of spinel-melilite-rich CAIs ((4.08±0.75)×10^{-5} to (5.05±0.18)×10^{-5}) are slightly lower than the canonical value of 5.25×10^{-5}. As most spinel-melilite-rich CAIs have no petrologic evidence for re-melting after condensation, the observed lower initial ^{26}Al/^{27}Al ratios indicate either condensation of refractory phases occurred up to ~0.3 Ma after canonical CAIs or they formed before ^{26}Al was homogeneously distributed in the Solar nebula.

A pyroxene-anorthite-rich CAI, G92, has an ^{16}O-rich signature (Δ^{17}O=−23.3±0.3‰), like other CAIs. However, the relatively low (^{26}Al/^{27}Al)$_0$ of G92 anorthite ((5.21±0.54)×10^{-6}), indicates it formed by a reaction between primary melilite and ^{16}O-rich nebular gas approximately 2.3 Ma after CAI formation. The oxygen and magnesium isotope signatures suggest the existence of ^{16}O-rich gas in an environment devoid of ferromagnesian dust. This environment was present during the timing of chondrule formation.

Finally, averaged oxygen isotope ratios of refractory inclusions are distributed along the CCAM line and the PCM line, which is the regression line based on oxygen isotope data from Acfer 094 chondrules. Since the PCM line also overlaps with oxygen isotope data of extremely ^{16}O-poor cosmic symplectites (Δ^{17}O~83‰), the linear relationship among these materials is interpreted to represent mixing of two endmember components in the solar nebula: that of ^{16}O-rich solar nebular gas, and that of extremely ^{16}O-poor (or ^{17,18}O-rich) primordial volatiles.

Acknowledgements

We thank John W. Valley and Michael J. Spicuzza for oxygen isotope analyses of standards by a laser fluorination and gas-source mass spectrometry, John Fournelle for assistance with EPMA analysis, and Jim Kern for technical assistance with SIMS operation. We are grateful to Dr. K. Nagashima, an anonymous reviewer, and the associate editor Dr. A. N. Krot for constructive review comments and suggestions. This work is supported by the NASA Cosmochemistry program (NNX07AI46G, NNX11AG62G, NTK). WiscSIMS is partly supported by NSF (EAR03-19230, EAR07-44079, EAR10-53466).

Figure captions

Figure 1: Backscattered electron images of spinel-melilite-rich CAIs (a) G5, (b) G16, (c) G49, (d) G104, (e) Y81020-E-8, and enlarged views of (f) a large nodule in G16, (g) a small nodule in G16, (h) the melilite-rich interior of G104, and (i) the spinel layer in Y81020-E-8. Scale bars indicate 100 μm for (a) to (e), 50 μm for (f) to (h), and 20 μm for (i), respectively. Abbreviations: mel=melilite, sp=spinel, an=anorthite, di=(Al-Ti-rich) diopside, ol=olivine, and pv=perovskite

Figure 2: Backscattered electron images of (a) diopside-anorthite-rich CAI G92, and (b) enlarged view of G92. Scale bars indicate 100 μm for (a) and 50 μm for (b), respectively. Abbreviations are same as Fig. 1.

Figure 3: Backscattered electron images of AOAs (a) G17, (b) G28, (c) G44, (d) G58, and enlarged views of (e) anorthite-free Ca-, Al-rich domain in G17, (f) anorthite-bearing Ca-, Al-rich domains in G44. Scale bars indicate 100 μm for (a) to (d) and 50 μm for (e) and (f), respectively. Abbreviations are the same as in Fig. 1

Figure 4: Oxygen three-isotope diagrams. All the measured data in this study are shown in (a). A dotted rectangle at the lower left in (a) indicates the upper limit of the ranges of the enlarged views, (b) to (k). Diagrams from individual spinel-melilite-rich CAIs (sp-mel CAIs) include Y81020-E-8 (b), G5 (c), G16 (d), G49 (e), G104 (f). G92 (g) is a pyroxene-anorthite-rich CAI (px-an CAI). AOAs include G17 (h), G28 (i), G44 (j), G58 (k). Reference lines are Terrestrial Fractionation (TF, continuous line in (a)), Carbonaceous Chondrite Anhydrous Mineral (CCAM, dashed line), Primitive Chondrule Mineral (PCM, solid line), and Young and Russell (Y&R, gray solid line). Errors are 95% confidence.

Figure 5: Comparison of (a) $\Delta^{17}O$ and (b) $\delta^{18}O_{VSMOW}$ values between averaged values of individual CAIs and their rims. CAIs data are shown in ascending order of average $\Delta^{17}O$ values. Errors are 95% confidence.

Figure 6: ^{26}Al-^{26}Mg isotope systematics of (a) Y81020-E-8, (b) G5, (c) G49, (d) and (e) G16, (f) G104, (g) and (h) G92, (i) G17. Inferred $(^{26}Al/^{27}Al)_0$ values are shown. Formulae of individual regression lines are provided in Table 2. Similar scales of X and Y axes are applied to each plot for proper comparisons of slopes from individual regression lines. Errors are 95% confidence.

Figure 7: $(^{26}\text{Al}/^{27}\text{Al})_0$ vs. Δ^{17}Oof thesamples (CAIsandAOA) studied. Filledgraycircles aredata from fivespinel- melilite-richCAIsG5,G16,G49,G104,andY-81020-E-8. Open squaresaredatafrom AOAsG17,G28,G44,andG58.Two filledblackcircles represent $(^{26}\text{Al}/^{27}\text{Al})_0$ valuesofthediopside-melilite(5.2×10^{-5})andthemelilite-anorthite(5.2×10^{-6}) systems in CAI G92. Chondrule data from Acfer 094 reported by [1] Ushikubo et al. (2012) and[2]Ushikuboetal.(2013) arealsoshown forcomparison. Verticaldottedline indicatesthecanonicalvalueof($^{26}\text{Al}/^{27}\text{Al})_0$ (5.25×10^{-5}). Errorsare95%confidence.

Figure 8: Oxygenthree-isotope plots of(a)averagevaluesofindividualCAIsandAOAs and(b)individual AOA analyseswithalargeprimarybeamandmultiple-FCdetectors. Errorsare95%confidence.

Figure9: Oxygenthree-isotopeplotsofrefractoryinclusions(averagedvaluesofCAIs andAOAs,thisstudy),chondrules(averagedvaluesandindividualrelictolivinedata, Ushikuboetal.,2012),and cosmicsymplectites(spot analysis dataofCOS,Sakamotoet al.,2007)fromAcfer094. FourreferencelinesaresameasFig. 4.

References:

Alexander C. M. O'D. (2004) Chemical equilibrium and kinetic constraints for chondrule and CAI formation conditions. *Geochim. Cosmochim. Acta* **68**, 3943-3969.

Bodénan J.-D., Starkey N. A., Russell S. S., Wright I. P., and Franchi I. A. (2014) An oxygen isotope study of Wark-Lovering rims on type A CAIs in primitive carbonaceous chondrites. *Earth Planet. Sci. Lett.* **401**, 327-336.

Ciesla F. J. (2005) Chondrule-forming processes – An overview. In Chondrites and the protoplanetary disk. ASP Conference Series, Vol. 341 (eds. A. N. Krot, E. R. D. Scott, and B. Reipurth). Astronomical Society of the Pacific, San Francisco, pp. 811-820.

Ciesla F. J. (2009) Two-dimensional transport of solids in viscous protoplanetary disks. *Icarus*, **200**, 655-671.

Ciesla F. J. (2010) The distributions and ages of refractory objects in the solar nebula. *Icarus* **208**, 455-467.

Clayton R. N. (2003) Oxygen isotopes in meteorites. In *Treatise on Geochemistry 1*, Meteorites, Comets, and Planets (ed. A. M. Davis). Elsevier-Pergamon, Oxford, pp. 129-142.

Clayton R. N. and Mayeda T. K. (1977) Correlated oxygen and magnesium isotope anomalies in Allende inclusions, I: Oxygen. *Geophys. Res. Lett.* **4**, 295-298.

Clayton R. N., Mayeda T. K., Goswami J. N., and Olsen E. J. (1991) Oxygen isotope studies of ordinary chondrites. *Geochim. Cosmochim. Acta* **55**, 2317-2337.

Clayton R. N., Mayeda T. K., Hutcheon I. D., Molini-Velsko C., Onuma N., Ikeda Y., and Olsen E. J. (1983) Oxygen isotopic compositions of chondrules in Allende and ordinary chondrites. In *Chondrules and their origins* (ed. E. A. King). Lunar Planet. Inst., Houston, TX, pp. 37-43.

Clayton R. N., Onuma N., Grossman L., and Mayeda T. K. (1977) Distribution of the pre-solar component in Allende and other carbonaceous chondrites. *Earth Planet. Sci. Lett.* **34**, 209-224.

Connolly Jr. H. C. and Huss G. R. (2010) Compositional evolution of the protoplanetary disk: Oxygen isotopes of type-II chondrules from CR2 chondrites. *Geochim. Cosmochim. Acta* **74**, 2473-2483.

Desch S. J., Morris M. A., Connolly Jr. H. C., and Boss A. P. (2012) The importance of experiments: Constraints on chondrule formation models. *Meteorit. Planet. Sci.* **47**, 1139-1156.

Ebel D. S. and Grossman L. (2000) Condensation in dust-enriched systems. *Geochim. Cosmochim. Acta* **64**, 339-366.

Eiler J. M. (2001) Oxygen isotope variations of basaltic lavas and upper mantle rocks. In Reviews in mineralogy and geochemistry 43, Stable isotope geochemistry (Eds. J. W. Valley, D. R. Cole). The mineralogical society of America, Washington DC, pp. 319-364.

Fedkin A. V. and Grossman L. (2006) The fayalite content of chondritic olivine: Obstacle to understanding the condensation of rocky material. In *Meteorites and the Early Solar System II* (eds. D. S. Lauretta and H. Y. McSween). Univ. of Arizona Press, Tucson, pp. 279-294.

Fedkin A. V. and Grossman L. (2016) Effects of dust enrichment on oxygen fugacity of cosmic gases. *Meteorit. Planet. Sci.* **51**, 843-850.

Fagan T. J., Guan Y., and MacPherson G. J. (2007) Al-Mg isotopic evidence for episodic alteration of Ca-Al-rich inclusions from Allende. *Meteorit. Planet. Sci.* **42**, 1221-1240.

Fagan T. J., Krot A. N., Keil K., and Yurimoto H. (2004) Oxygen isotopic evolution of amoeboid olivine aggregates in the reduced CV3 chondrites Efremovka, Vigarano, and Leoville. *Geochim. Cosmochim. Acta* **68**, 2591-2611.

Goswami J. N., Srinivasan G., and Ulyanov A. A. (1994) Ion microprobe studies of Efremovka CAIs: I. Magnesium isotope composition. *Geochim. Cosmochim. Acta* **58**, 431-447.

Gounelle M., Krot A. N., Hagashima K., and Kearsley A. (2009) Extreme ^{16}O enrichment in calcium-aluminum-rich inclusions from the Isheyevo (CH/CB) chondrite. *Astrophys. J.* **698**, L18-L22.

Greshake A. (1997) The primitive matrix components of the unique carbonaceous chondrite Acfer 094: A TEM study. *Geochim. Cosmochim. Acta* **61**, 437-452.

Grossman L. (1972) Condensation in the primitive solar nebula. *Geochim. Cosmochim. Acta* **36**, 597-619.

Grossman J. N. and Brearley A. J. (2005) The onset of metamorphism in ordinary and carbonaceous chondrites. *Meteorit. Planet. Sci.* **40**, 87-122.

Grossman L. and Ganapathy R. (1976) Trace elements in the Allende meteorite–II. Fine-grained, Ca-rich inclusions. *Geochim. Cosmochim. Acta* **40**, 967-977.

Grossman L., Simon S. B., Rai V. K., Thiemens M. H., Hutcheon I. D., Williams R. W., Galy A., Ding T., Fedkin A. V., Clayton R. N., Mayeda T. K. (2008) Primordial compositions of refractory inclusions. *Geochim. Cosmochim. Acta* **72**, 3001-3021.

Grossman L. and Steele I. M. (1976) Amoeboid olivine aggregates in the Allende meteorite. *Geochim. Cosmochim. Acta* **40**, 149-155.

Hashimoto A. (1992) The effect of H_2O gas on volatilities of planet-forming major elements: I. Experimental determination of thermodynamic properties of Ca-, Al-, and Si-hydroxide gas molecules and its application to the solar nebula. *Geochim. Cosmochim. Acta* **56**, 511-532.

Heck P. R., Ushikubo T., Schmitz B., Kita N. T., Spicuzza M. J., and Valley J. W. (2010) A single asteroidal source for extraterrestrial Ordovician chromite grains from Swede n and China: High-precision oxygen three-isotope SIMS analysis. *Geochim. Cosmochim. Acta* **74**, 497-509.

Hiyagon H., and Hashimoto A. (1999) ^{16}O Excesses in Olivine Inclusions in Yamato-86009 and Murchison Chondrites and Their Relation to CAIs. *Science* **283**, 828-831.

Hsu W., Wasserburg G. J., Huss G. R. (2000) High time resolution by use of the ^{26}Al

chronometer in the multistage formation of a CAI. *Earth Planet Sci. Lett.* **182**, 15-29.

Hutcheon I. D., Marhas K. K., Krot A. N., Goswami J. N., and Jones R. H. (2009) ^{26}Al in plagioclase-rich chondrules in carbonaceous chondrites: Evidence for an extended duration of chondrule formation. *Geochim. Cosmochim. Acta* **73**, 5080-5099.

Jacobsen B., Han J. M., Matzel J. E., Brearley A. J., Hutcheon I. D. (2014) Oxygen isotopes in Fine-grained spinel-pyroxene and melilite-rich CAIs in the ALHA 77307 CO3.0 carbonaceous chondrite. *Lunar Planet. Sci. XLV*. #2789 (abstr.).

Jacobsen B., Yin Q.-Z., Moyner F., Amelin Y., Krot A. N., Nagashima K., Hutcheon I. D., Palme H. (2008) ^{26}Al-^{26}Mg and ^{207}Pb-^{206}Pb systematics of Allende CAIs: Canonical solar initial ^{26}Al/^{27}Al ratio reinstated. *Earth Planet Sci. Lett.* **272**, 353-364.

Jacquet E. (2013) On vertical variations of gas flow in protoplanetary disks and their impact on the transport of solids. *Astron. Astrophys.* **551**, A75.

Kawasaki N., Kato C., Itoh S., Wakaki S., Ito M., and Yurimoto H. (2015) 26Al-26Mg chronology and oxygen isotope disturbance of multiple melting for a type C CAI from Allende. *Geochim. Cosmochim. Acta* **169**, 99-114.

Kimura M., Grossman J. N., and Weisberg M. K. (2008) Fe-Ni metal in primitive chondrites: Indicators f classification and metamorphic conditions for ordinary and CO chondrites. *Meteorit. Planet. Sci.* **43**, 1161-1177.

Kita N. T., Nagahara H., Tachibana S., Tomomura S., Spicuzza M. J., Fournelle J. H., Valley J. W. (2010) High precision SIMS oxygen three isotope study of chondrules in LL3 chondrites: Role of ambient gas during chondrule formation. *Geochim. Cosmochim. Acta* **74**, 6610-6635.

Kita N. T., and Ushikubo T. (2012) Evolution of protoplanetary disk inferred from ^{26}Al chronology of individual chondrules. *Meteorit. Planet. Sci.* **47**, 1108-1119.

Kita N. T., Ushikubo T., Fu B., and Valley J. W. (2009) High precision SIMS oxygen isotope analysis and the effect of sample topography. *Chem. Geol.* **264**, 43-57.

Kita N. T., Ushikubo T., Knight K. B., Mendybaev R. A., Davis A. M., Richter F. M., and Fournelle J. H. (2012) Internal ^{26}Al-^{26}Mg isotope systematics of a Type B CAI: Remelting of refractory precursor solids. *Geochim. Cosmochim. Acta* **86**, 37-51.

Kita N. T., Yin Q.-Z., MacPherson G. J., Ushikubo T., Jacobsen B., Nagashima K., Kurahashi E., Krot A. N., Jacobsen S. B. (2013) ^{26}Al-^{26}Mg isotope systematics of the first solids in the early solar system. *Meteorit. Planet. Sci.* **48**, 1383-1400.

Kobayashi S., Imai H., and Yurimoto H. (2003) New extreme ^{16}O-rich reservoir in the early solar system. *Geochem. J.* **37**, 663-669.

Kööp L., Nakashima D., Heck P. R., Kita N. T., Tenner T. J., Krot A. N., Nagashima K., Park C., and Davis A. M. (2016) New constraints on the relationship between 26Al and oxygen, calcuim, and titanium isotopic variation in the early Solar System from a multielement isotopis study of spinel-hibonite inclusions. *Geochim. Cosmochim. Acta* **184**, 151-172.

Krot A. N., Chaussidon M., Yurimoto H., Sakamoto N., Nagashima K., Hutcheon I. D., and MacPherson G. J. (2008) Oxygen isotopic compositions of Allende type C CAIs: Evidence for isotopic exchange during nebular melting and asteriodal metamorphism. *Geochim. Cosmochim. Acta* **72**, 2534-2555.

Krot A. N., Fagan T. J., Keil K., McKeegan K. D., Sahijpal S. Hutcheon I. D., Petaev M. I., and Yurimoto H. (2004a) Ca, Al-rich inclusions, amoeboid olivine aggregates, and Al-rich chondrules from the unique carbonaceous chondrite Acfer 094: I. Mineralogy and petrology. *Geochim. Cosmochim. Acta* **68**, 2167-2184.

Krot A. N., MacPherson G. J., Ulyanov A. A., and Petaev M. I. (2004b) Fine-grained, spinel-rich inclusions from the reduced CV chondrites Efremovka and Leoville: I. Mineralogy, petrology, and bulk chemistry. *Meteorit. Planet. Sci.* **39**, 1517-1553.

Krot A. N., McKeegan K. D., Leshin L. A., MacPherson G. J., Scott E. R. D. (2002) Existence of an ^{16}O-rich gaseous reservoir in the solar nebula. *Science*, **295**, 1051-1054.

Krot A. N., Nagashima K., Ciesla F. J., Meyer B. S., Hutcheon I. D., Davis A. M., Huss G. R., and Scott E. R. D. (2010a) Oxygen isotopic composition of the Sun and mean oxygen isotopic composition of the protosolar silicate dust: Evidence from refractory inclusions. *Astrophys. J.* **713**, 1159-1166.

Krot A. N., Nagashima K., van Kooten E. M. M. E., and Bizzarro M. (2016) High-temperature rims around calcium-aluminum-rich inclusions from the CR, CB, and CH carbonaceous chondrites. *Lunar Planet. Sci. XLVII.* # 1203 (abstr.).

Krot A. N., Nagashima K., Yoshitake M., and Yurimoto H. (2010b) Oxygen isotopic compositions of chondrules from the metal-rich chondrites isheyevo (CH/CB$_b$), MAC 02675 (CB$_b$) and QUE 94627 (CB$_b$). *Geochim. Cosmochim. Acta* **74**, 2190-2211.

Krot A. N., Nagashima K., Wasserburg G. J., Huss G. R., Papanastassiou D., Davis A. M., Hutcheon I. D., Bizzarro M. (2014a) Calcium-aluminum-rich inclusions with fractionation and unknown nuclear effects (FUN CAIs): I. Mineralogy, petrology, and oxygen isotopic compositions. *Geochim. Cosmochim. Acta* **145**, 206-247.

Krot A. N., Park C., and Nagashima K. (2014b) Amoeboid olivine aggregates from CH carbonaceous chondrites. *Geochim. Cosmochim. Acta* **139**, 131-153.

Kunihiro T., Rubin A. E., McKeegan K. D., Wasson J. T. (2004) Initial ^{26}Al/^{27}Al in carbonaceous-chondrite chondrules: Too little ^{26}Al to melt asteroids. *Geochim. Cosmochim. Acta* **68**, 2947-2957.

Kurahashi E., Kita N. T., Nagahara H., and Morishita Y. (2008) ^{26}Al-^{26}Mg systematics of chondrules in a primitive CO chondrite. *Geochim. Cosmochim. Acta* **72**, 3865-3882.

Larsen K. K., Trinquier A., Paton C., Schiller M., Wielandt D., Ivanova M. A., Connelly J. N., Nordlund Å., Krot A. N., Bizzarro M. (2011) Evidence for magnesium isotope heterogeneity in the solar protoplanetary disk. *Astropys. J. Lett.* **735**, L37 (7pp).

Lodders K. (2003) Solar system abundances and condensation temperatures of the elements. *Astrophys. J.* **591**, 1220-1247.

MacPherson G. J., Kita N. T., Ushikubo T., Bullock E. S., and Davis A. M. (2012) Well-resolved variations in the formation ages for Ca-Al-rich inclusions in the early Solar System. *Earth Planet Sci. Lett.* **331-332**, 43-54.

Makide K., Nagashima K., Krot A. N., Huss G. R., Hutcheon I. D., and Bischoff A. (2009) Oxygen- and magnesium-isotope compositions of calcium-aluminum-rich inclusions from CR2 carbonaceous chondrites. *Geochim. Cosmochim. Acta* **73**, 5018-5050.

McKeegan K. D., Kallio A. P. A., Heber V. S., Jarzebinski G., Mao P. H., Coath C. D., Kunihiro T., Wiens R. C., Nordholt J. E., Moses Jr. R. W., Resenfeld D. B., Jurewicz A. J. G., and Burnett D. S. (2011) The Oxygen Isotopic Composition of the Sun Inferred from Captured Solar Wind. *Science* **332**, 1528-1532.

Nakamura T., Noguchi T., Tsuchiyama A., Ushikubo T., Kita N. T., Valley J. W., Zolensky M. E., Kakazu Y., Sakamoto K., Mashio E., Uesugi K., and Nakano T. (2008) Chondrulelike Objects in Short-Period Comet 81P/Wild2. *Science* **321**, 1664-1667.

Nakashima D., Ushikubo T., Joswiak D. J., Brownlee D. E., Matrajt G., Weisberg M. K., Zolensky M. E., and Kita N. T. (2012) Oxygen isotopes in crystalline silicates of comet Wild 2: A comparison of oxygen isotope systematics between Wild 2 particles and chondritic materials. *Earth Planet. Sci. Lett.* **357-358**, 355-365.

Podosek F. A., Zinner E. K., MacPherson G. J., Lundberg L. L., Brannon J. C., Fahey A. J. (1991) Correlated study of initial ^{87}Sr/^{86}Sr and Al-Mg isotopic systematics and petrologic properties in a suite of refractory inclusions from the Allende meteorite. *Geochim. Cosmochim. Acta* **55**, 1083-1110.

Rudraswami N. G., Ushikubo T., Nakashima D., and Kita N. T. (2011) Oxygen isotope systematics of chondrules in the Allende CV3 chondrite: High precision ion microprobe studies. *Geochim. Cosmochim. Acta* **75**, 7596-7611.

Sakamoto N., Seto Y., Itoh S., Kuramoto K., Fujino K., Nagashima K., Krot A. N., Yurimoto H. (2007) Remnants of the early solar system water enriched in heavy oxygen isotopes. *Science*, **317**, 231-233.

Schrader D. L., Connolly Jr. H. C., Lauretta D. S., Nagashima K., Huss G. R., Davidson J., Domanik K. J. (2013) The formation and alteration of the Renazzo-like carbonaceous chondrites II: Linking O-isotope composition and oxidation state of chondrule olivine. *Geochim. Cosmochim. Acta* **101**, 302-327.

Schrader D. L., Nagashima K., Krot A. N., Ogliore R. C., and Hellebrand E. (2014) Variations in the O-isotope composition of gas during the formation of chondrules from the CR chondrites. *Geochim. Cosmochim. Acta* **132**, 50-74.

Scott E. R. D., Love S. G., and Krot A. N. (1996) Formation of chondrules and chondrites in the protoplanetary nebula. In *Chondrules and the Protoplanetary Disk* (eds. R. H. Hewins, R. Jones, and E. R. D. Scott). Cambridge Univ. Press, Cambridge, pp. 87-96.

Seto Y., Sakamoto N., Fujino K. Kaito T., Oikawa T., and Yurimoto H. (2008) Mineralogical characterization of a unique material having heavy oxygen isotope anomaly in matrix of the primitive carbonaceous chondrite Acfer 094. *Geochim. Cosmochim. Acta* **72**, 2723-2734.

Simon J. I., Matzel J. E. P., Simon S. B., Hutcheon I. D., Ross D. K., Weber P. K., and Grossman L. (2016) Oxygen isotopic variations in the outer margins and Wark-Lovering rims of refractory inclusions. *Geochim. Cosmochim. Acta* **186**, 242-276.

Simon J. I., Hutcheon I. D., Simon S. B., Matzel J. E. P., Ramon E. C., Weber P. K., Grossman L., and DePaolo D. J. (2011) Oxygen isotope variations at the margin of a CAI records circulation within the solar nebula. *Science* **331**, 1175-1178.

Tenner T. J., Nakashima D., Ushikubo T., Kita N. T., and Weisberg M. K. (2015) Oxygen isotope ratios of FeO-poor chondrules in CR3 chondrites: Influence of dust enrichment and H_2O during chondrule formation. *Geochim. Cosmochim. Acta* **148**, 228-250.

Tenner T. J., Ushikubo T., Kurahashi E., Kita N. T., and Nagahara H. (2013) Oxygen isotope systematics of chondrule phenocrysts from the CO3.0 chondrite Yamato 81020: Evidence for two distinct oxygen isotope reservoirs. *Geochim. Cosmochim. Acta* **102**, 226-245.

Ushikubo T., Guan Y., Hiyagon H., Sugiura N., and Leshin L. A. (2007) ^{36}Cl, ^{26}Al, and O isotopes in an Allende type B2 CAI: Implications for multiple secondary alteration events in the early solar system. *Meteorit. Planet. Sci.* **42**, 1267-1279.

Ushikubo T., Kimura M., Kita N. T., and Valley J. W. (2012) Primordial oxygen isotope reservoirs of the solar nebula recorded in chondrules in Acfer 094 carbonaceous chondrite. *Geochim. Cosmochim. Acta* **90**, 242-264.

Ushikubo T., Nakashima D., Kimura M., Tenner T. J., and Kita N. T. (2013) Contemporaneous formation of chondrules in distinct oxygen isotope reservoirs. *Geochim. Cosmochim. Acta* **109**, 280-295.

Wang J., Davis A. M., Clayton R. N., Mayeda T. K., Hashimoto A. (2001) Chemical and isotopic fractionation during the evaporation of the FeO-MgO-SiO_2-CaO-Al_2O_3-TiO_2 rare earth element melt system. *Geochim. Cosmochim. Acta* **65**, 479-494.

Wark D., and Boynton W. V. (2001) The formation of rims on calcium-aluminum-rich inclusions: Step I – Flash heating. *Meteorit. Planet. Sci.* **36**, 1135-1166.

Wark D. A. and Lovering J. F. (1977) Marker events in the early evolution of the solar system: Evidence from rims on Ca-Al-rich inclusions in carbonaceous chondrites. *Proc. Lunar Sci. Conf.* **8**, 95-112.

Wasserburg G. J., Lee T., and Papanastassiou D. A. (1977) Correlated O and Mg isotopic anomalies in Allende inclusions: II. Magnesium. *Geophys. Res. Lett.* **4**, 299-302.

Weisberg M. K., Ebel D. S., Connolly Jr. H. C., Kita N. T., Ushikubo T. (2011) Petrology and oxygen isotope compositions of chondrules in E3 chondrites. *Geochim. Cosmochim. Acta* **75**, 6556-6569.

Yoshitake M., Koide Y., and Yurimoto H. (2005) Correlations between oxygen-isotopic composition and petrologic setting in a coarse-grained Ca, Al-rich inclusion. *Geochim. Cosmochim. Acta* **69**, 2663-2674.

Yurimoto H., Ito M., and Nagasawa H. (1998) Oxygen isotope exchange between refractory inclusion in Allende and Solar Nebula gas. *Science* **282**, 1874-1877.

Yurimoto H., Kuramoto K., Krot A. N., Scott E. R. D., Cuzzi J. N., Thiemens M. H., Lyons J. R. (2007) Origin and evolution of oxygen isotopic compositions of the Solar System. In Protostars and planets V (eds. B. Reipurth, D. Jewitt, K. Keil). The University of Arizona press, Tuscon, AZ, pp.849-862.

Figure 1

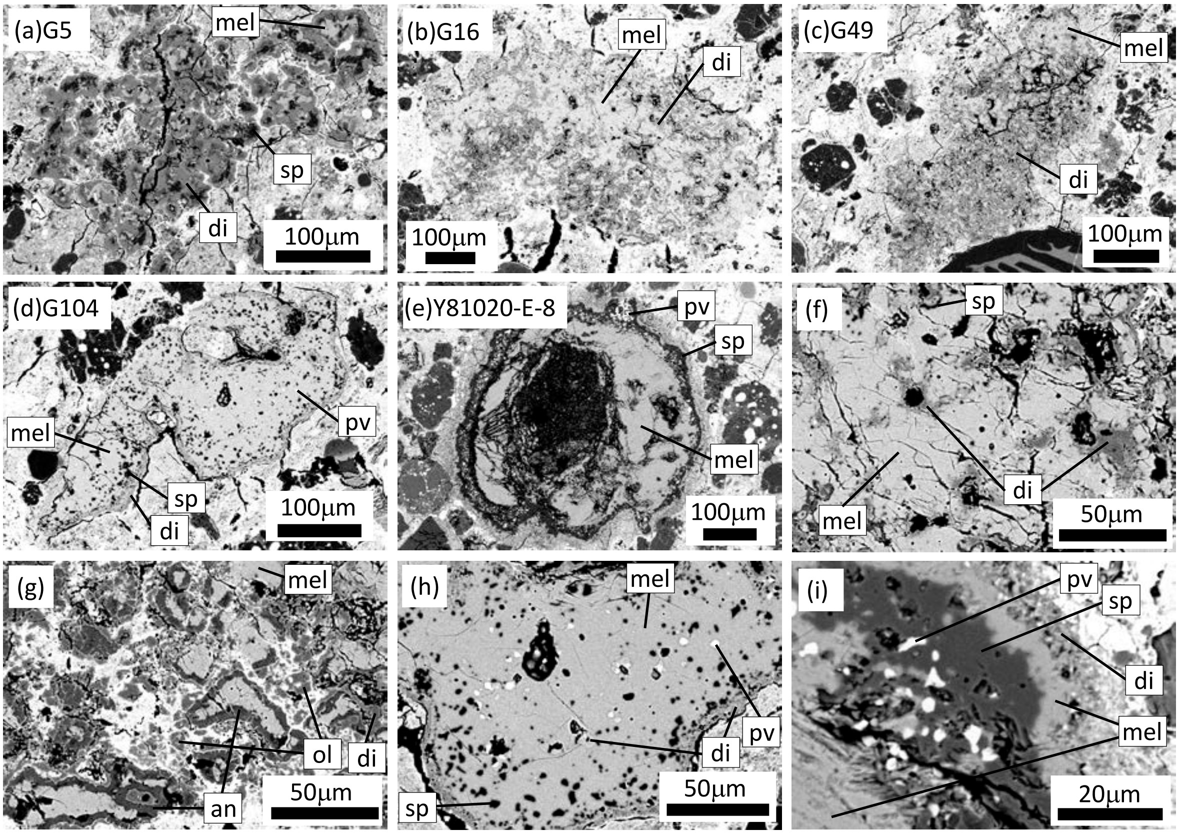
(a)G5
mel
sp
di
100μm
(b)G16
mel
di
100μm
(c)G49
mel
di
100μm
(d)G104
pv
mel
sp
di
100μm
(e)Y81020-E-8
pv
sp
mel
100μm
(f)
sp
mel
di
50μm
(g)
mel
ol
di
an
50μm
(h)
mel
pv
di
sp
50μm
(i)
pv
sp
di
mel
20μm

Figure 2

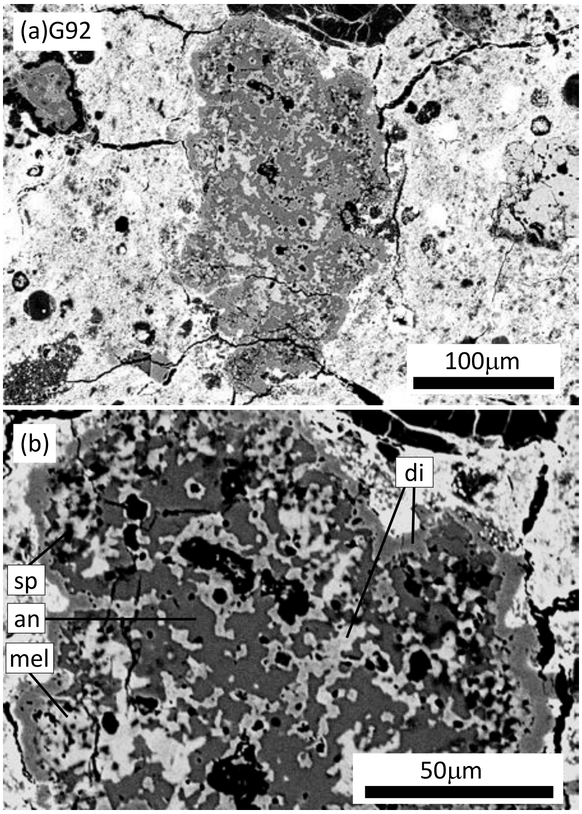

Figure 3

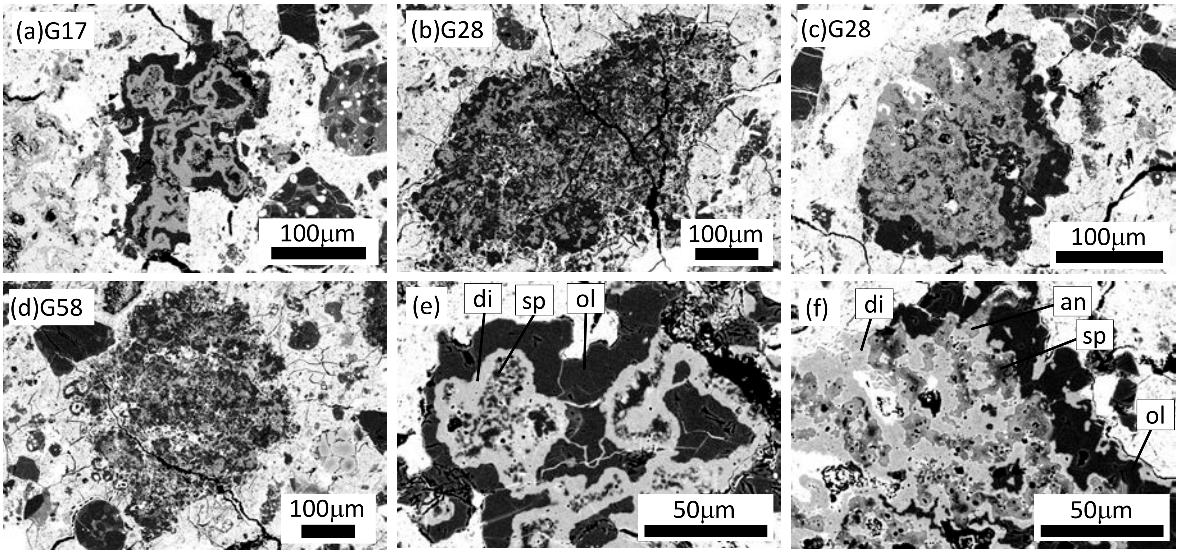
(a)G17
100μm
(b)G28
100μm
(c)G28
100μm
(d)G58
100μm
(e)
di
sp
ol
50μm
(f)
di
an
sp
ol
50μm

Figure 4

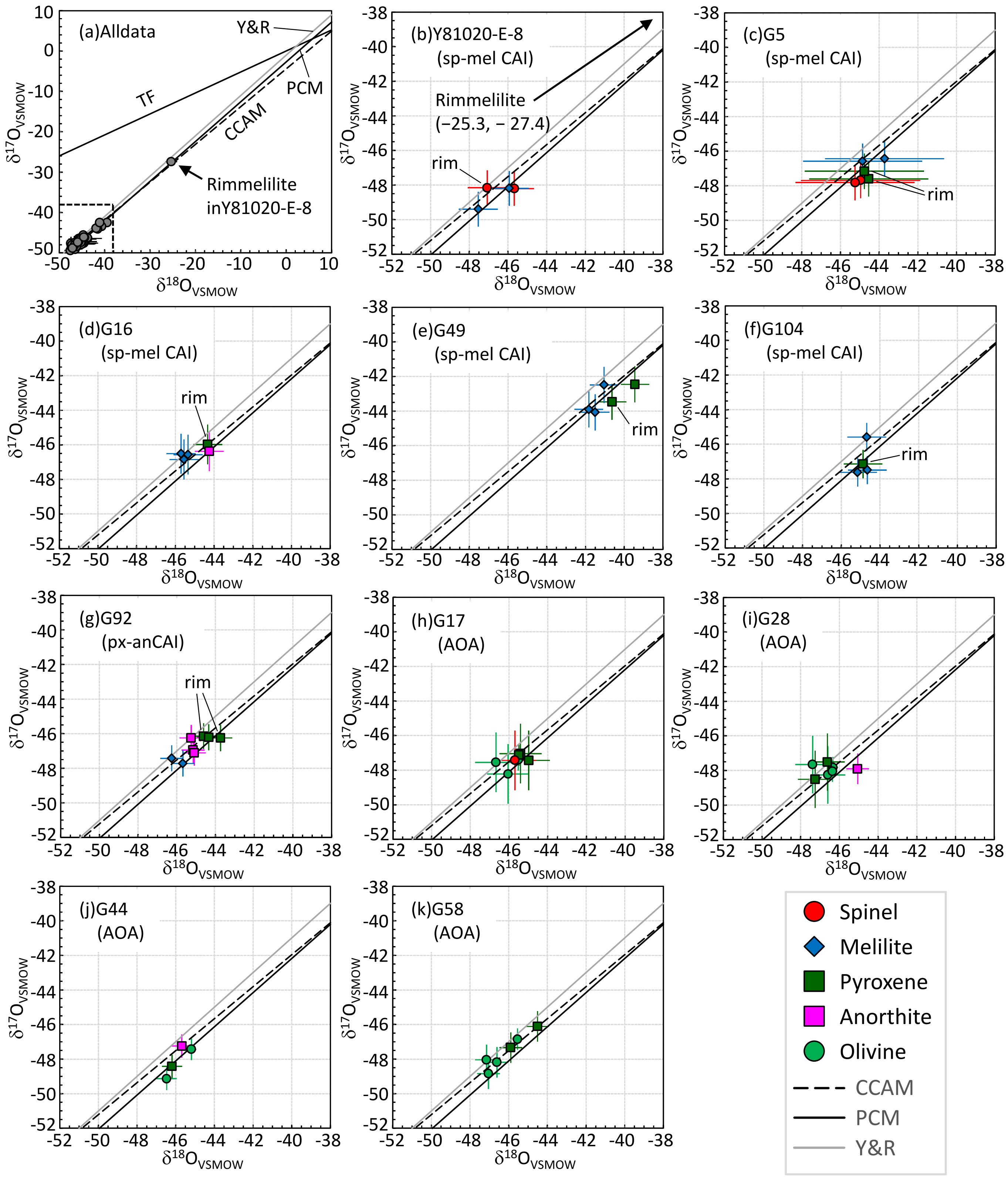

(a)Alldata
Y&R
TF
PCM
CCAM
Rimmelilite
inY81020-E-8
(b)Y81020-E-8
(sp-mel CAI)
Rimmelilite
(−25.3, − 27.4)
rim
(c)G5
(sp-mel CAI)
rim
(d)G16
(sp-mel CAI)
rim
(e)G49
(sp-mel CAI)
rim
(f)G104
(sp-mel CAI)
rim
(g)G92
(px-anCAI)
rim
(h)G17
(AOA)
(i)G28
(AOA)
(j)G44
(AOA)
(k)G58
(AOA)
$\delta^{17}O_{VSMOW}$
$\delta^{18}O_{VSMOW}$
10
0
-10
-20
-30
-40
-50
-38
-40
-42
-44
-46
-48
-50
-52
Spinel
Melilite
Pyroxene
Anorthite
Olivine
CCAM
PCM
Y&R

Figure 5

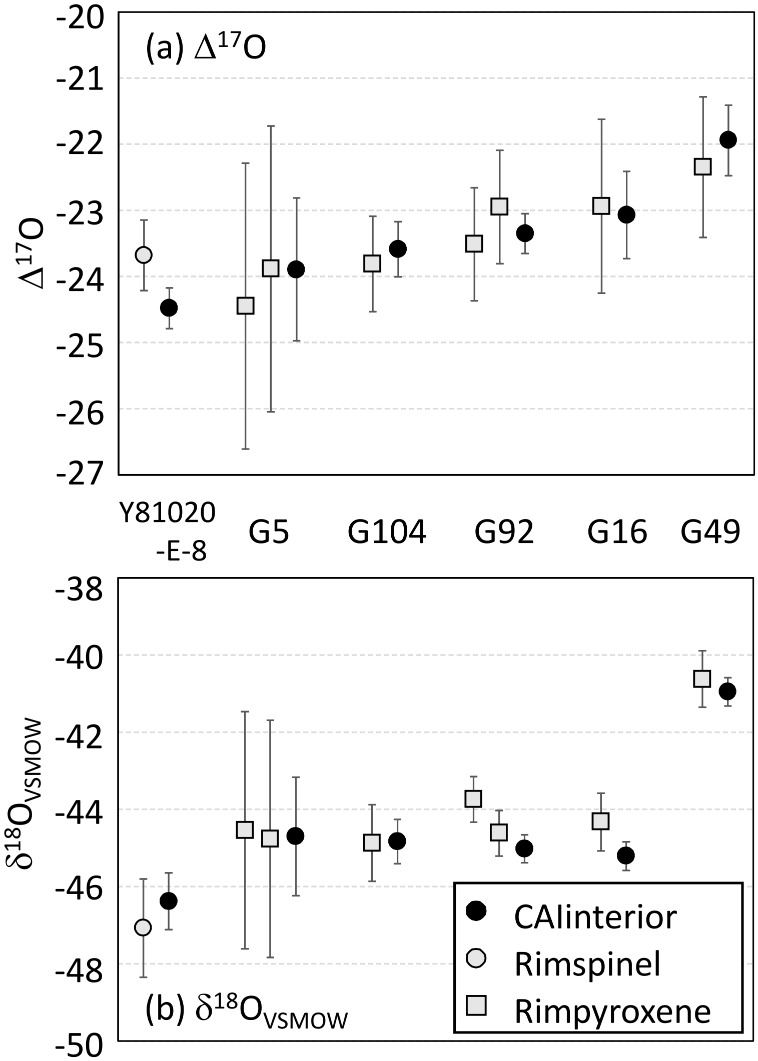
(a) Δ^{17}O
Δ^{17}O
-20
-21
-22
-23
-24
-25
-26
-27
Y81020
-E-8
G5
G104
G92
G16
G49
(b) δ^{18}O$_{VSMOW}$
δ^{18}O$_{VSMOW}$
-38
-40
-42
-44
-46
-48
-50
CAlinterior
Rimspinel
Rimpyroxene

Figure 6

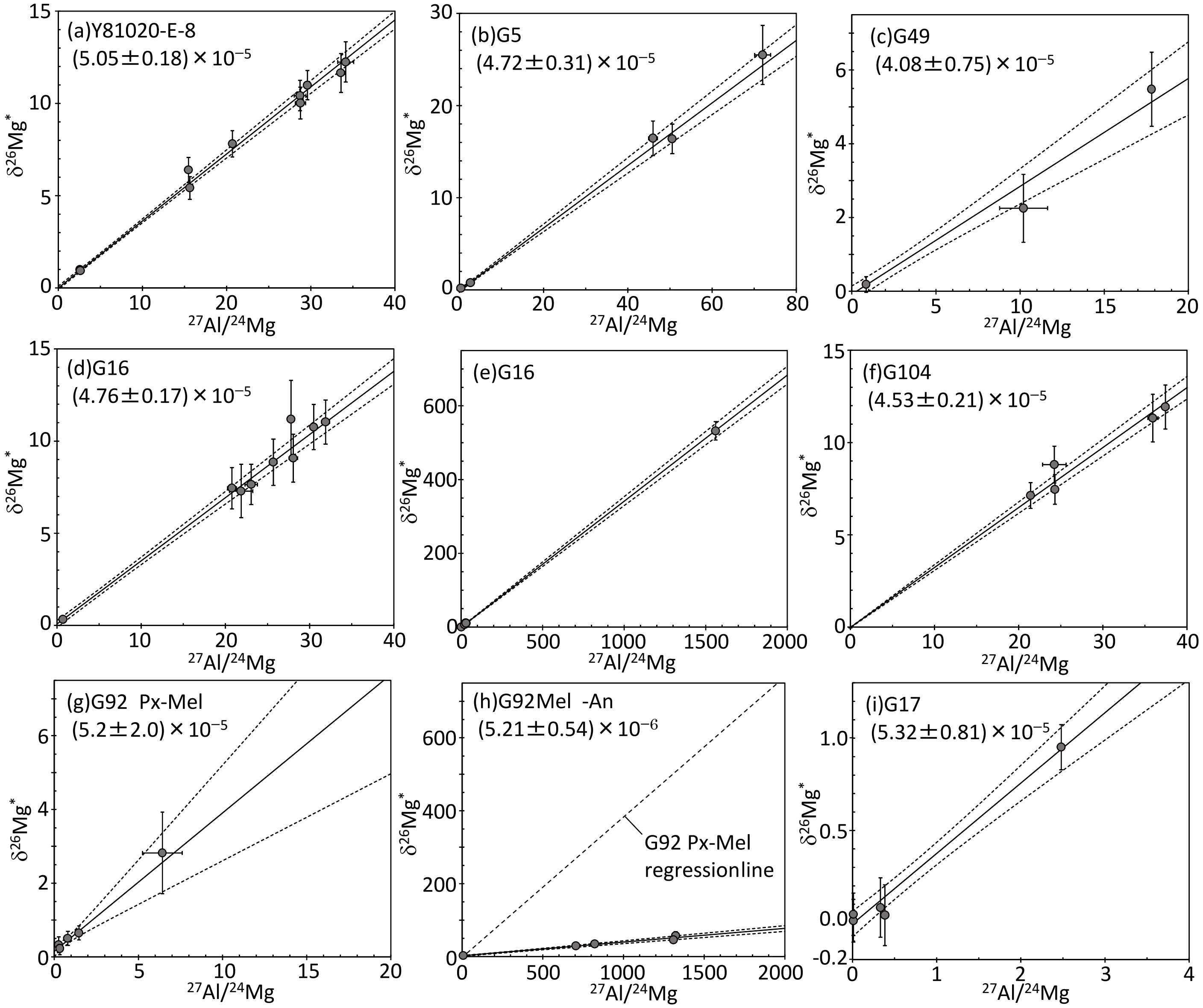

(a)Y81020-E-8
(5.05±0.18)×10⁻⁵
(b)G5
(4.72±0.31)×10⁻⁵
(c)G49
(4.08±0.75)×10⁻⁵
(d)G16
(4.76±0.17)×10⁻⁵
(e)G16
(f)G104
(4.53±0.21)×10⁻⁵
(g)G92 Px-Mel
(5.2±2.0)×10⁻⁵
(h)G92Mel -An
(5.21±0.54)×10⁻⁶
G92 Px-Mel regressionline
(i)G17
(5.32±0.81)×10⁻⁵
δ26Mg*
27Al/24Mg

Figure 7

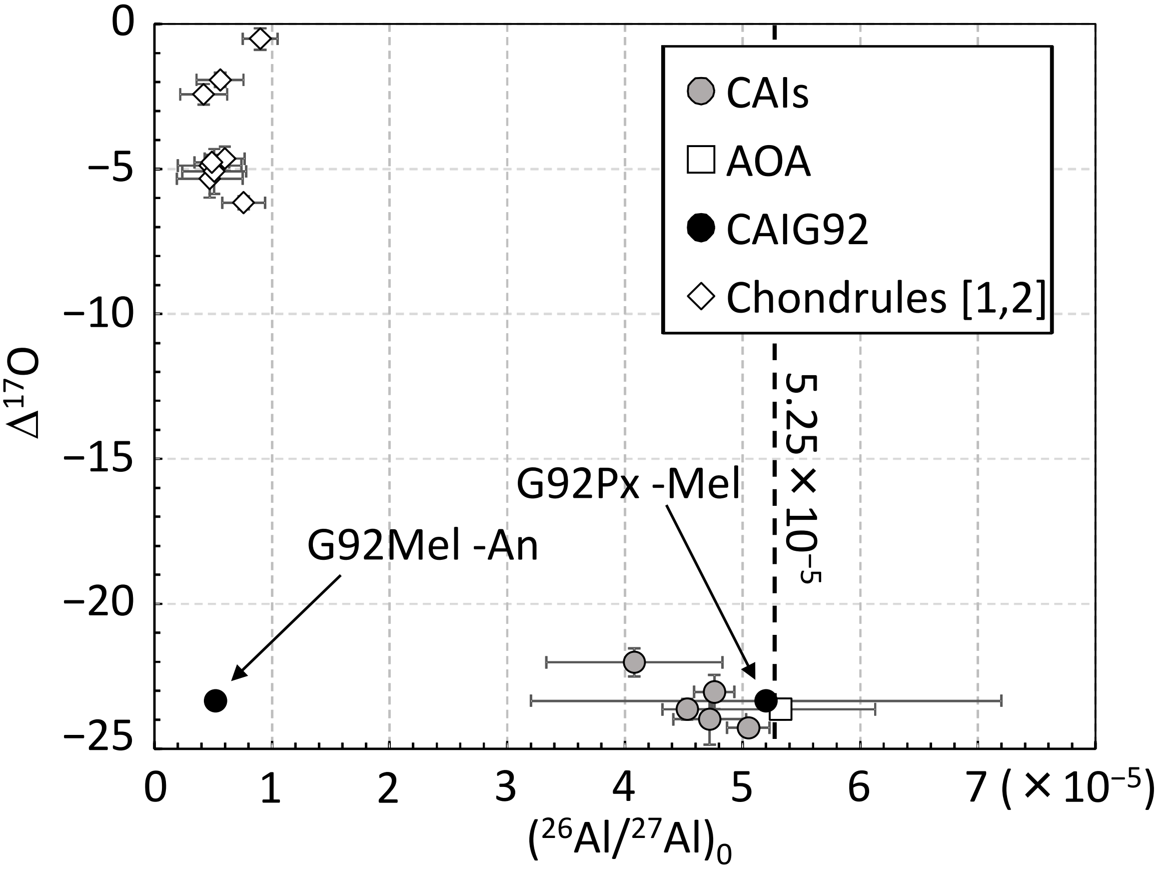

CAIs
AOA
CAIG92
Chondrules [1,2]
$\Delta^{17}O$
0
−5
−10
−15
−20
−25
0
1
2
3
4
5
6
7 (× 10⁻⁵)
$(^{26}Al/^{27}Al)_0$
G92Mel -An
G92Px -Mel
5.25 × 10⁻⁵

Figure 8

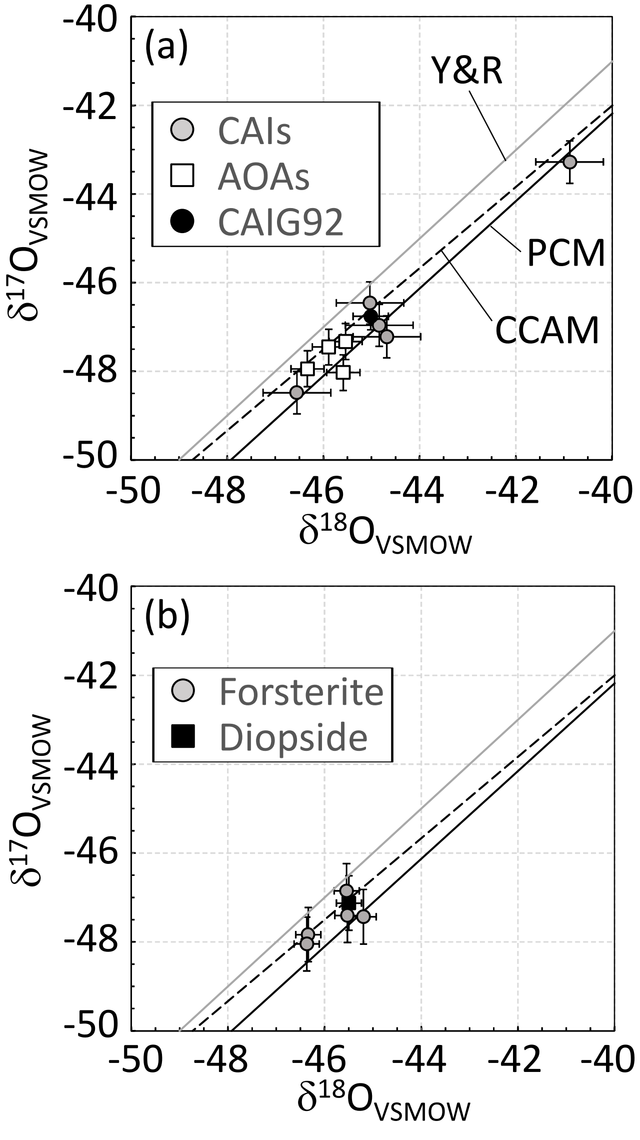
(a)
Y&R
PCM
CCAM
CAIs
AOAs
CAIG92
-40
-42
-44
-46
-48
-50
-50
-48
-46
-44
-42
-40
$\delta^{17}O_{VSMOW}$
$\delta^{18}O_{VSMOW}$
(b)
Forsterite
Diopside
-40
-42
-44
-46
-48
-50
-50
-48
-46
-44
-42
-40
$\delta^{17}O_{VSMOW}$
$\delta^{18}O_{VSMOW}$

Figure 9

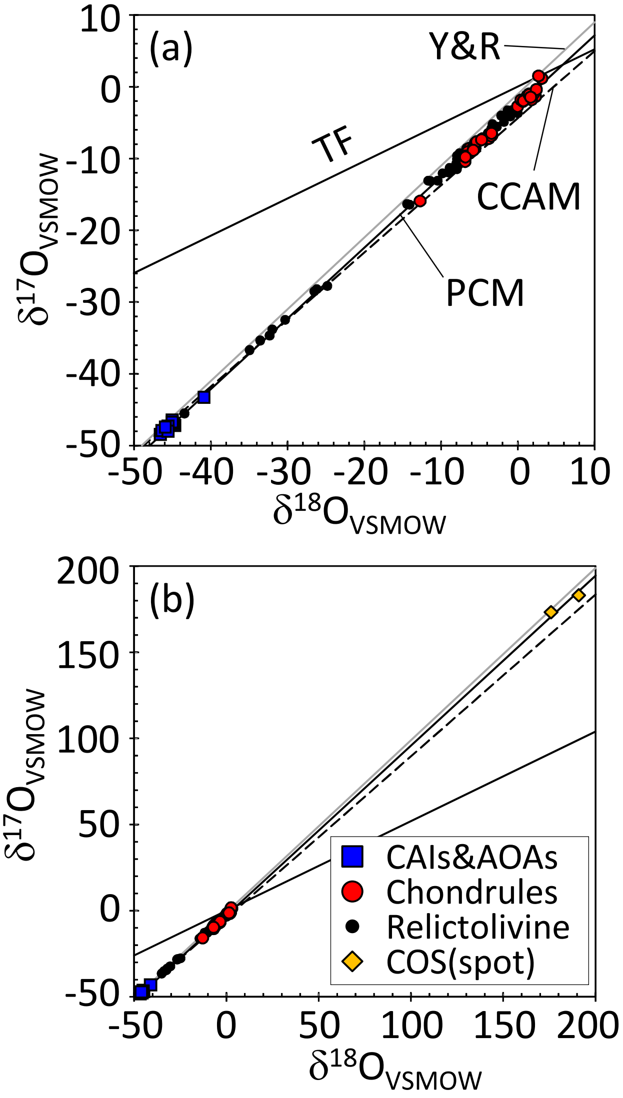
(a)
Y&R
TF
CCAM
PCM
10
0
-10
-20
-30
-40
-50
-50
-40
-30
-20
-10
0
10
$\delta^{17}O_{VSMOW}$
$\delta^{18}O_{VSMOW}$
(b)
200
150
100
50
0
-50
-50
0
50
100
150
200
$\delta^{17}O_{VSMOW}$
$\delta^{18}O_{VSMOW}$
CAIs&AOAs
Chondrules
Relictolivine
COS(spot)

Table 1: Oxygen isotope ratios of Refractory Inclusions from Acfer 094.

Sample/Analysis #[a]	Phase[b]	$\delta^{18}O_{VSMOW}$ (‰)	(2 SE)	$\delta^{17}O_{VSMOW}$ (‰)	(2 SE)	$\Delta^{17}O$ (‰)	(2 SE)	Note
CAIs								
Y81020-E-8								
#62	Sp	-45.7	±1.3	-48.2	±0.9	-24.5	±0.5	
#63	Sp (rim)	-47.1	±1.3	-48.2	±0.9	-23.7	±0.5	
#61	Mel	-45.9	±1.3	-48.2	±0.9	-24.3	±0.5	
#66	Mel	-47.5	±1.3	-49.4	±0.9	-24.7	±0.5	
#67	Mel (rim)	-25.3	±1.3	-27.4	±0.9	-14.3	±0.5	
Average[c]		-46.6	±0.7	-48.5	±0.5	-24.3	±0.3	excluding #67
G5								
#75	Fas (rim)	-44.5	±3.1	-47.6	±1.0	-24.4	±2.2	
#77	Fas (rim)	-44.8	±3.1	-47.2	±1.0	-23.9	±2.2	
#72	Sp	-45.0	±3.1	-47.7	±1.0	-24.3	±2.2	
#74	Sp	-45.3	±3.1	-47.8	±1.0	-24.3	±2.2	
#73	Mel	-43.7	±3.1	-46.4	±1.0	-23.7	±2.2	
#76	Mel	-44.9	±3.1	-46.6	±1.0	-23.3	±2.2	
Average[c]		-44.7	±1.3	-47.2	±0.4	-24.0	±0.9	
G16								
#84	Fas (rim)	-44.3	±0.7	-46.0	±1.1	-22.9	±1.3	
#83	Mel	-45.7	±0.7	-46.5	±1.1	-22.7	±1.3	
#86	Mel	-45.3	±0.7	-46.6	±1.1	-23.0	±1.3	
#87	Mel	-45.5	±0.7	-46.8	±1.1	-23.2	±1.3	
#82	An	-44.2	±0.7	-46.4	±1.1	-23.4	±1.3	
Average[c]		-45.0	±0.4	-46.5	±0.5	-23.0	±0.6	
G49								
#94	Fas	-39.4	±0.7	-42.5	±1.0	-21.9	±1.1	
#97	Fas (rim)	-40.6	±0.7	-43.5	±1.0	-22.3	±1.1	
#93	Mel	-41.5	±0.7	-44.1	±1.0	-22.5	±1.1	
#95	Mel	-41.8	±0.7	-43.9	±1.0	-22.2	±1.1	
#98	Mel	-41.0	±0.7	-42.5	±1.0	-21.2	±1.1	
Average[c]		-40.9	±0.4	-43.3	±0.5	-22.0	±0.5	
G92								
#105	Fas (rim)	-43.7	±0.6	-46.3	±0.7	-23.5	±0.9	
#108	Fas (rim)	-44.6	±0.6	-46.1	±0.7	-22.9	±0.9	
#110	Fas	-44.3	±0.6	-46.2	±0.7	-23.1	±0.9	
#106	Mel	-45.7	±0.6	-47.7	±0.7	-24.0	±0.9	
#107	Mel	-46.3	±0.6	-47.4	±0.7	-23.4	±0.9	
#103	An	-45.3	±0.6	-46.3	±0.7	-22.7	±0.9	
#104	An	-45.2	±0.6	-47.0	±0.7	-23.5	±0.9	
#109	An	-45.1	±0.6	-47.1	±0.7	-23.7	±0.9	
Average[c]		-45.0	±0.4	-46.8	±0.3	-23.3	±0.3	
G104								
#119	Fas (rim)	-44.9	±1.0	-47.1	±0.8	-23.8	±0.7	
#115	Mel	-44.7	±1.0	-47.5	±0.8	-24.3	±0.7	
#118	Mel	-45.2	±1.0	-47.6	±0.8	-24.1	±0.7	
#120	Mel	-44.7	±1.0	-45.6	±0.8	-22.3	±0.7	
Average[c]		-44.8	±0.6	-47.0	±0.4	-23.6	±0.4	
AOAs								
G17								
#129	Fo	-46.1	±1.1	-48.2	±1.7	-24.3	±1.4	
#130	Fo (edge)	-46.7	±1.1	-47.5	±1.7	-23.3	±1.4	
#316 (2nd session)[d]	Fo (edge)	-45.5	±0.3	-47.4	±0.6	-23.7	±0.6	
#128	Fas	-45.0	±1.1	-47.4	±1.7	-24.0	±1.4	
#131	Fas	-45.4	±1.1	-47.0	±1.7	-23.4	±1.4	
#315 (2nd session)[d]	Fas	-45.5	±0.3	-47.1	±0.6	-23.5	±0.6	
#127	Sp	-45.7	±1.1	-47.4	±1.7	-23.7	±1.4	
Average[c]		-45.5	±0.3	-47.3	±0.4	-23.6	±0.4	
G28								
#137	Fo (edge)	-46.6	±0.9	-48.3	±1.6	-24.0	±1.5	
#140	Fo	-47.4	±0.9	-47.7	±1.6	-23.0	±1.5	
#317 (2nd session)[d]	Fo (edge)	-46.3	±0.3	-47.8	±0.6	-23.7	±0.6	
#318 (2nd session)[d]	Fo (edge)	-46.4	±0.3	-48.0	±0.6	-23.9	±0.6	
#138	Fas	-46.6	±0.9	-47.5	±1.6	-23.3	±1.5	
#142	Fas	-47.3	±0.9	-48.5	±1.6	-23.9	±1.5	
#163	An	-45.1	±0.6	-47.9	±0.9	-24.5	±0.9	
Average[c]		-46.3	±0.3	-47.9	±0.4	-23.9	±0.3	
G44								
#148	Fo (edge)	-46.5	±0.5	-49.1	±0.7	-25.0	±0.8	
#319 (2nd session)[e]	Fo (edge)	-45.2	±0.3	-47.4	±0.6	-23.9	±0.6	
#150	Fas	-46.2	±0.5	-48.4	±0.7	-24.4	±0.8	
#151	An	-45.7	±0.5	-47.2	±0.7	-23.5	±0.8	
Average[c]		-45.6	±0.4	-48.0	±0.4	-24.2	±0.4	
G58								
#157	Fo	-47.1	±0.6	-48.0	±0.9	-23.5	±0.9	
#159	Fo	-46.6	±0.6	-48.2	±0.9	-23.9	±0.9	
#160	Fo	-47.0	±0.6	-48.8	±0.9	-24.4	±0.9	
#320 (2nd session)[d]	Fo (edge)	-45.5	±0.3	-46.8	±0.6	-23.2	±0.6	
#162	Fas	-45.9	±0.6	-47.3	±0.9	-23.5	±0.9	
#158	Fas	-44.5	±0.6	-46.1	±0.9	-23.0	±0.9	
Average[c]		-45.9	±0.4	-47.5	±0.4	-23.5	±0.3	

a: Analysis points are shown in Fig. EA2.

b: Abbreviations: Sp=spinel, Mel=melilite, Fas=Al-Ti-rich diospide, An=anorthite, Fo=forsteritic olivine.

c: Uncertainty of $\Delta^{17}O$ is the error of the weighted mean value. Additional uncertainties of the instrumen

d: Multiple-FCs analysis with a high intensity beam.

Table 2: Al–Mg isotope systematics of Refractory Inclusions from Acfer 094

Sample/Analysis#[a]	Phase[b]	$\delta^{25}Mg_{DSM3}$ (2 SE) (‰/amu)		$^{27}Al/^{24}Mg$ (2 SE)		$\delta^{26}Mg^*$ (2 SE) (‰)		Note
CAIs								
Y81020-E-8								
#100 (2nd session)[c]	Sp (rim)	1.17	±0.14	2.583	±0.027	0.99	±0.14	
#101 (2nd session)[c]	Sp (rim)	1.31	±0.14	2.637	±0.027	0.93	±0.11	
#9,10[d]	Mel	1.21	±0.47	29.62	±0.29	10.99	±0.79	average
#11	Mel	0.95	±0.62	34.17	±0.95	12.25	±1.09	
#12,13[d]	Mel	-1.38	±0.43	20.70	±0.24	7.82	±0.71	average
#14	Mel	-0.93	±0.39	15.65	±0.15	5.42	±0.62	
#15	Mel	-0.09	±0.50	28.74	±0.70	10.42	±0.83	
#16	Mel	0.36	±0.43	15.47	±0.21	6.40	±0.68	
#17	Mel	0.82	±0.59	33.59	±0.47	11.66	±1.06	
#18	Mel	-1.36	±0.50	28.79	±0.60	10.02	±0.86	
average & isochron[e]		**0.21**	**±2.16**	$\delta^{26}Mg^*=(0.363\pm0.013)\times(^{27}Al/^{24}Mg)+(0.01\pm0.10)$				
				$(^{26}Al/^{27}Al)_0=(5.05\pm0.18)\times10^{-5}$				
G5								
#78 (2nd session)[c]	Fas (rim)	-0.94	±0.28	0.337	±0.006	0.18	±0.20	
#77 (2nd session)[c]	Sp	-0.78	±0.28	2.624	±0.027	0.80	±0.16	
#52	Mel	-1.22	±1.60	72.01	±1.86	25.48	±3.21	100 cycles
#53	Mel	2.87	±0.88	50.55	±0.55	16.38	±1.60	
#56	Mel	-1.13	±1.01	45.98	±1.01	16.45	±1.87	100–300 c
average & isochron[e]		**-0.24**	**±3.50**	$\delta^{26}Mg^*=(0.339\pm0.022)\times(^{27}Al/^{24}Mg)-(0.03\pm0.13)$				
				$(^{26}Al/^{27}Al)_0=(4.72\pm0.31)\times10^{-5}$				
G16								
#80 (2nd session)[c]	Fas	-1.18	±0.28	0.717	±0.008	0.33	±0.19	
#20	Mel	0.47	±0.67	28.06	±0.50	9.08	±1.30	
#21	Mel	0.08	±0.65	31.90	±0.48	11.04	±1.20	
#22	Mel	-0.71	±1.03	27.79	±0.21	11.19	±2.11	41–150 cy
#23	Mel	-0.63	±0.61	20.77	±0.52	7.45	±1.12	
#24	Mel	-0.36	±0.60	23.07	±0.72	7.65	±1.09	
#25	Mel	0.14	±0.68	25.69	±0.45	8.86	±1.25	
#26	Mel	0.41	±0.86	21.87	±1.38	7.29	±1.45	
#28	Mel	-1.46	±0.62	30.48	±0.26	10.76	±1.23	
#29	An	0.30	±8.90	1561	±16	532	±25	1–19 cycle
average & isochron[e,f]		**-0.36**	**±1.38**	$\delta^{26}Mg^*=(0.342\pm0.012)\times(^{27}Al/^{24}Mg)+(0.09\pm0.18)$				
				$(^{26}Al/^{27}Al)_0=(4.76\pm0.17)\times10^{-5}$				
G49								
#82 (2nd session)[c]	Fas	-0.13	±0.28	0.859	±0.028	0.19	±0.21	
#48	Mel	1.09	±0.56	17.82	±0.17	5.48	±1.01	
#50	Mel	2.24	±0.56	10.21	±1.43	2.25	±0.92	
average & isochron[e]		**1.07**	**±2.37**	$\delta^{26}Mg^*=(0.293\pm0.054)\times(^{27}Al/^{24}Mg)-(0.08\pm0.22)$				
				$(^{26}Al/^{27}Al)_0=(4.08\pm0.75)\times10^{-5}$				
G92								
#69 (2nd session)[c]	Fas (rim)	-0.44	±0.24	0.271	±0.012	0.33	±0.21	
#70 (2nd session)[c]	Fas	-0.55	±0.24	1.472	±0.048	0.65	±0.19	
#71 (2nd session)[c]	Fas	-0.63	±0.24	0.807	±0.021	0.50	±0.19	
#72 (2nd session)[c]	Fas (rim)	-0.39	±0.24	0.335	±0.011	0.23	±0.16	
#38	Mel	1.03	±0.71	6.43	±1.17	2.82	±1.10	
#33	An	2.69	±5.82	1324	±14	58	±12	1–85 cycle
#34	An	1.83	±4.09	1310	±14	46.0	±8.7	
#36	An	3.15	±2.90	822.5	±8.7	34.8	±5.2	
#37	An	9.74	±4.26	705.9	±7.7	29.4	±8.0	1–100 cycl
average & isochron[e,f]		**-0.19**	**±1.38**	$\delta^{26}Mg^*=(0.38\pm0.14)\times(^{27}Al/^{24}Mg)+(0.15\pm0.14)$				Fas&Mel
				$(^{26}Al/^{27}Al)_0=(5.2\pm2.0)\times10^{-5}$				Fas&Mel
				$\delta^{26}Mg^*=(0.0374\pm0.0039)\times(^{27}Al/^{24}Mg)+(2.6\pm1.1)$				Mel&An
				$(^{26}Al/^{27}Al)_0=(5.21\pm0.54)\times10^{-6}$				Mel&An
G104								
#40	Mel	1.09	±0.68	37.43	±0.42	11.94	±1.19	
#41	Mel	0.91	±0.56	24.23	±1.41	8.81	±0.99	
#44	Mel	1.37	±0.68	35.94	±0.62	11.33	±1.29	1–211 cycl
#46	Mel	1.53	±0.48	24.31	±0.33	7.46	±0.80	
#47	Mel	1.56	±0.40	21.42	±0.16	7.13	±0.70	
average & isochron[e]		**1.29**	**±0.56**	$\delta^{26}Mg^*=(0.325\pm0.015)\times(^{27}Al/^{24}Mg)-(0.03\pm0.01)$				Assuming t
				$(^{26}Al/^{27}Al)_0=(4.53\pm0.21)\times10^{-5}$				
AOAs								
G17								
#64 (2nd session)[c]	Fo (rim)	0.36	±0.24			0.01	±0.12	
#65 (2nd session)[c]	Fo (rim)	0.59	±0.24			0.04	±0.12	
#66 (2nd session)[c]	Fas	-0.37	±0.24	0.332	±0.005	0.08	±0.16	
#68 (2nd session)[c]	Fas	-0.36	±0.24	0.385	±0.006	0.04	±0.16	
#67 (2nd session)[c]	Sp	0.98	±0.24	2.480	±0.027	0.95	±0.12	
average & isochron[e]		**0.24**	**±1.19**	$\delta^{26}Mg^*=(0.381\pm0.058)\times(^{27}Al/^{24}Mg)-(0.006\pm0.069)$				
				$(^{26}Al/^{27}Al)_0=(5.32\pm0.81)\times10^{-5}$				
G28								
#83 (2nd session)[c]	Fo (rim)	0.68	±0.28			0.04	±0.16	
#84 (2nd session)[c]	Fo (rim)	0.34	±0.28			0.07	±0.16	
average[e]		**0.51**	**±0.48**			**0.06**	**±0.12**	
G44								
#89 (2nd session)[c]	Fo (rim)	1.12	±0.13			0.00	±0.08	
#92 (2nd session)[c]	Fo (rim)	0.92	±0.13			0.03	±0.08	
average & isochron[e]		**1.02**	**±0.28**			**0.02**	**±0.06**	
G58								
#93 (2nd session)[c]	Fo (rim)	0.65	±0.13			0.08	±0.07	
#94 (2nd session)[c]	Fo	0.55	±0.13			0.08	±0.09	
average & isochron[e]		**0.60**	**±0.13**			**0.08**	**±0.06**	

a: Analysis points are shown in Fig. EA2.
b: Abbreviations; Sp=spinel, Mel=melilite, Fas=Al–Ti–rich diospide, An=anorthite, Fo=forsteritic olivine.
c: Multiple–FCs analysis with a high intensity beam.
d: Average value of two analyses at the same analysis spot.
e: Errors are 2 SD for $\delta^{25}Mg$ values and 95% confidence for isochrons
f: Anorthite data is not used to calculate the $\delta^{25}Mg$ value.
g: Error is 95% confidence of the weighted mean value.